with direct influx of the peptide into the cytosol. We also showed that attachment of the fluorescent moiety or a peptide tag derived from positions 98–106 of human influenza hemagglutinin (HAtag, YPYDVPDYA) significantly stimulated particle formation, suggesting that direct penetration of R12 is greatly accelerated by the attachment of hydrophobic cargo molecules. Moreover, an Alexa Fluor 488-labeled R4 peptide (R4-Alexa488) and Alexa Fluor 488-labeled Gly-Cys-amide (GC-Alexa488), which usually show very little internalization, translocated through the plasma membrane into the cytosol when coincubated with R12-HAtag, while causing no major cytotoxicity to the cells.

RESULTS

Time-lapse imaging of direct internalization of the R12-Alexa488 peptide into cells

The direct translocation of R12-Alexa488 into living HeLa cells, and subsequent distribution, were analyzed by confocal microscopy. The final concentration of R12-Alexa488 in the medium was 5 μmol/l, which corresponds to the threshold value in serum-free medium for accomplishing direct translocation into the cytosol.[16] The fluorescent signal for R12-Alexa488 was detected in the cytosol as early as a few minutes after the addition of the peptide to the culture medium, and was typically detected in more than 80% of cells within 15 minutes (Figure 1a, upper panels). Entry of the peptide into the cytosol was initiated at specific sites with strong fluorescent signals and then spread throughout the entire plasma membrane (arrows in Figure 1a; see also **Supplementary Figure S1** and **Supplementary Video S1**), as previously reported by us and others.[14–16]

Simultaneous observation of the peptide-treated cells by differential interference contrast microscopy revealed that the direct internalization of R12-Alexa488 was accompanied by the formation of small particle-like structures ~1–3 μm in diameter on the plasma membrane (see lower panels of Figure 1a; compare with the lower and upper panels (arrows) in Figure 1a). Note that the locations of these particles on the plasma membrane exactly coincided with the points of peptide influx (Figure 1a, upper panels). The topology of the particle structures was further analyzed by staining the cell membranes with the nonspecific membrane dye FM4-64 (see **Supplementary Figure S2**). Z-stack analysis of the particles showed excellent three-dimensional agreement with the R12-Alexa488 signals, suggesting the involvement of both membrane components and R12-Alexa488 in the formation of these particles. The influx of R12-Alexa488 at these specific sites was transient, with a typical duration of 10–20 minutes. The particles gradually became larger in size in response to influx of the peptide into cells (arrows in Figure 1a) and often retained their structure even after no further peptide influx was observed. Multiple sites of influx in individual cells were often formed in turn during treatment with R12-Alexa488 (as indicated by the arrows at 4 minutes in Figure 1a). In contrast, R4-Alexa488, which has only poor translocation ability, had no significant effect on the cellular membranes, even when applied at a threefold higher concentration (**Supplementary Figure S3b**), suggesting that the number of arginine residues may be a critical factor in the influx of peptides into cells.

Note that the influx sites for R12-Alexa488 were always accompanied by particulate membrane structures. Moreover, peptide influx and particle structure formation also occurred at low temperatures (4 °C and 15 °C) (Figure 1b and **Supplementary Figure S3a**), suggesting that these processes are energy-independent and thus probably do not require active transport machineries.[15] The energy independence of particle formation was further confirmed by assessing particle formation in the presence of macropinocytosis inhibitors. Macropinocytosis has been reported to be one of the major pathways for the internalization of arginine-rich peptides.[10] Treatment of cells with the representative macropinocytosis inhibitors EIPA and cytochalasin D (CytD) did not affect the induction of membrane particle formation by R12-Alexa488 (**Supplementary Figure S4**). Also, in the presence of EIPA, enhanced cytosolic penetration of the peptide through the plasma membrane was observed, consistent with the results of a previous study in which fluorescein-labeled R9 and Tat were used.[14] Many more membrane particles were formed in the presence of EIPA compared to control conditions, in accord with the enhanced influx of R12-Alexa488 into cells (**Supplementary Figure S4**). The above results further suggest that the diffusion of R12-Alexa488 into HeLa cells accompanying membrane particle

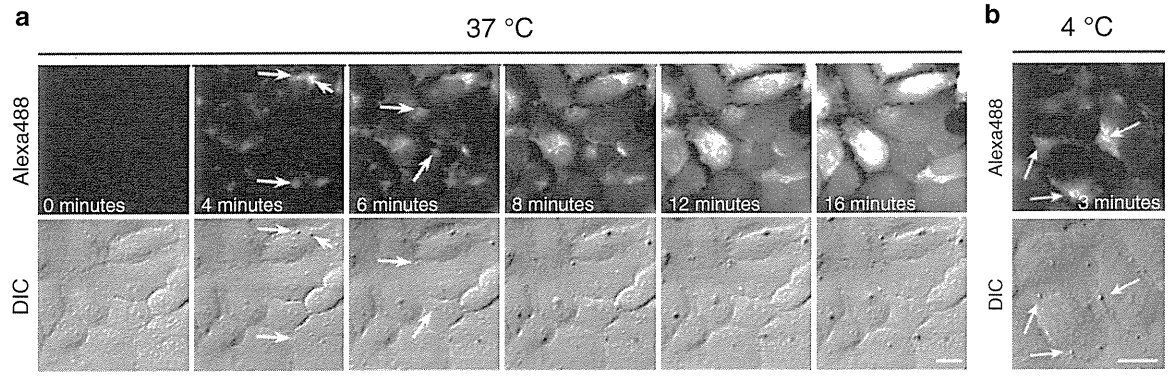

Figure 1 Direct internalization of R12-Alexa488 into the cytosol accompanied by the formation of particle-like structures on the plasma membrane. (**a**,**b**) Time-lapse images of cells incubated with R12-Alexa488 (5 μmol/l) in serum-free medium (α-MEM(–)) at (**a**) 37 °C and (**b**) 4 °C. Upper panels (labeled "Alexa488") show time-lapse fluorescence images for Alexa Fluor 488. Lower panels (labeled "DIC") present differential interference contrast (DIC) images of the same fields shown in the upper panels. Arrows indicate peptide influx points (fluorescence images for Alexa Fluor 488) and membrane particles (DIC images). Time 0: images captured immediately before the addition of R12-Alexa488. Bar = 20 μm. MEM, minimum essential medium.

formation is independent of energy-dependent cellular machineries, including macropinocytosis.

Membrane potential was previously reported to play a critical role in the internalization of arginine-rich peptides into cells.[7] We therefore examined whether particle formation was dependent on the membrane potential. Under physiological conditions, high Na^+ levels in the extracellular environment and high K^+ levels in the cytosol maintain a transmembrane potential. Replacement of Na^+ in the extracellular fluid with K^+ diminishes this transmembrane potential. We thus employed a K^+-rich buffer (K^+ concentration 140 mmol/l) as the extracellular medium (**Supplementary Figure S5a**).[17] When HeLa cells were incubated with R12-Alexa488 (5 μmol/l) in Na^+-rich buffer (Na^+ concentration 140 mmol/l), which maintained the normal membrane potential, membrane particles were formed as described above (**Supplementary Figure S5a**, upper panels). In contrast, significant particle formation and R12-Alexa488 influx into cells were not observed using the K^+-rich buffer (**Supplementary Figure S5a**, lower panels). Even when R12-Alexa488 was applied at a concentration of 20 μmol/l, no significant membrane particle formation was detected in the K^+-rich buffer (data not shown). These results suggest that membrane particle formation is affected by K^+ ion concentration, or the membrane potential. This was further confirmed by the recovery of R12-Alexa488 influx into cells and membrane particle formation when an excess of the Na^+-rich buffer was applied to cells that had initially been treated with the K^+-rich buffer (see **Supplementary Figure S5b**). These results strongly suggest that interaction of the peptide with cell surfaces is not sufficient for the formation of membrane particles, and that a membrane potential is required for the influx of R12-Alexa488 into cells via the plasma membrane.

Plasma membrane inversion accompanies R12 internalization

The influx of R12-Alexa488 through the plasma membrane may be accompanied by migration of the membrane and associated molecules, thereby leading to membrane inversion. Phosphatidylserine is a membrane component that under normal conditions is primarily localized to the inner side of the plasma membrane. Plasma membrane disorder, such as that induced by apoptosis, can lead to inversion of the membrane, and thus the presentation of phosphatidylserine at the cell surface. This can be detected with a specific binding partner, the protein annexin V.[11]

Significant signals for Alexa Fluor 568-labeled annexin V were detected in HeLa cells that had been coincubated with the R12-Alexa488 (Figure 2a). In addition, these annexin V signals were highly colocalized with both the sites of peptide influx and the particles that transiently formed on the membranes (Figure 2a, arrows). In contrast, no significant annexin V signals were detected in cells treated with the R4-Alexa488 (Figure 2b). These observations provide direct evidence that peptide treatment induces the dynamic movement of membrane molecules, accompanied by membrane inversion, in the extremely limited regions corresponding to the peptide influx sites. Note that although several phosphatidylserine signals in the outer cellular membrane were detected by annexin V staining, no apoptotic cell death was observed in cells treated with R12 under the described conditions (data not shown).

Accumulation of membrane-associated molecules to the sites of R12-Alexa488 internalization

The above results strongly suggest that the direct influx of R12-Alexa488 may be accompanied by the dynamic rearrangement of other membrane-associated molecules. Acidic membrane-associated molecules could realistically be expected to interact with the basic R12. We therefore monitored the dynamic behavior of the ganglioside GM1 following R12-Alexa488 treatment using Alexa Fluor 555-labeled cholera toxin subunit B (CTxB-Alexa555), a reagent that specifically binds to GM1,[18] a representative sialic glycolipid with one sialic acid moiety in its terminus. Strong CTxB signals were detected at sites of the peptide influx, and thus particle formation, in cells treated with R12-Alexa488 (Figure 3a). In contrast, no such signals were detected in cells treated with R4-Alexa488 (Figure 3b), suggesting that GM1 may interact with R12.

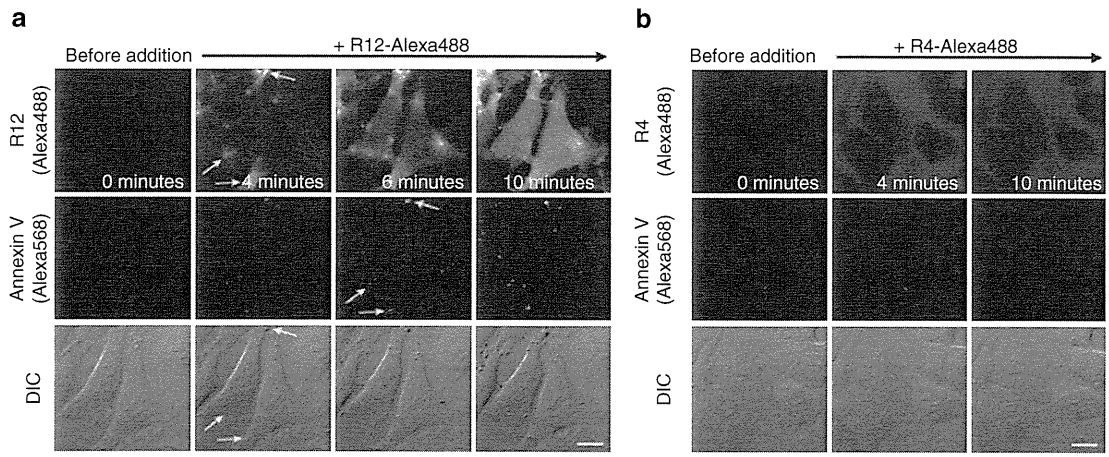

Figure 2 Membrane inversion coupled with influx of R12-Alexa488 into the cytosol. Time-lapse images of cells incubated with (**a**) R12-Alexa488 (5 μmol/l) or (**b**) R4-Alexa488 (15 μmol/l) in α-MEM(–) at 37 °C in the presence of annexin V-Alexa568. Upper, middle, and lower panels show fluorescent images of R12-Alexa488, fluorescent images of annexin V-Alexa568, and DIC images in the same fields, respectively. Arrows in **a** indicate sites of peptide influx (upper panel), annexin V signals (middle panel), and membrane particles (lower panel), respectively. Time 0: images captured immediately before the addition of the arginine peptides. Bar = 20 μm. DIC, differential interference contrast; MEM, minimum essential medium.

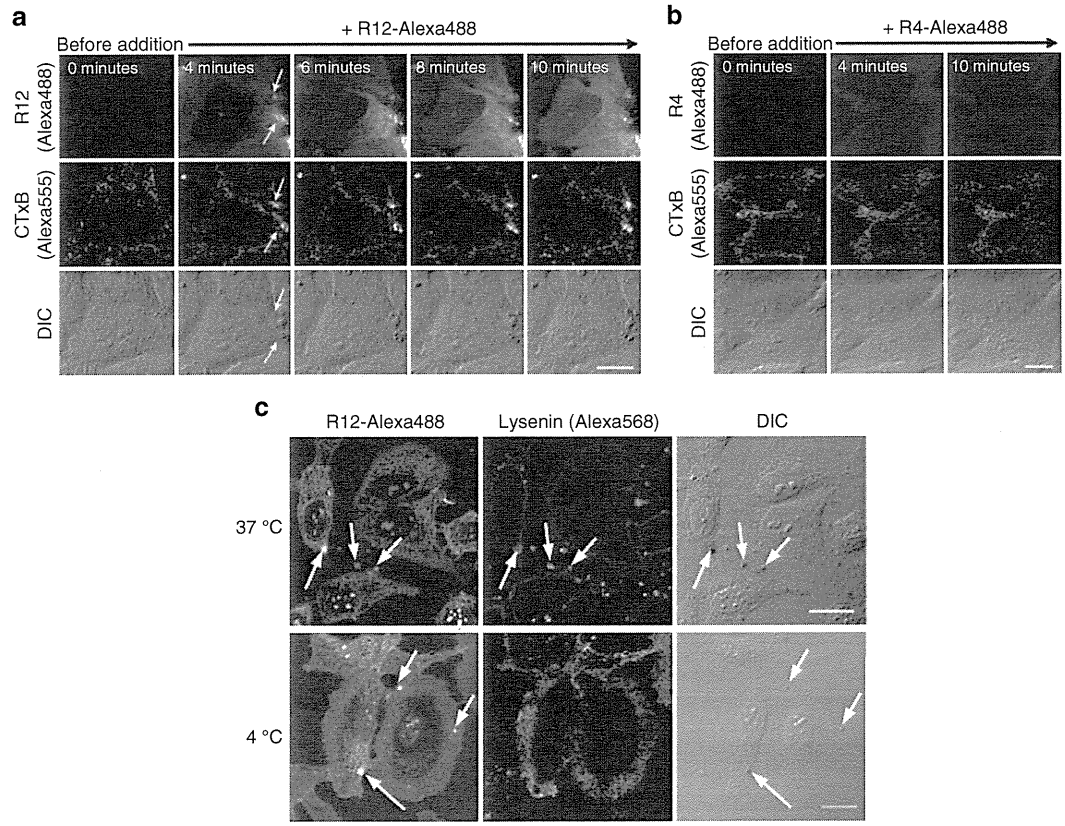

Figure 3 Recruitment of GM1 and sphingomyelin to the sites of peptide internalization. (**a**,**b**) Time-lapse images of cells incubated with 5 μmol/l (**a**) R12-Alexa488 or (**b**) R4-Alexa488 in serum-free medium (α-MEM(–)) at 37 °C. The arrows in **a** indicate sites of cholera toxin subunit B (CTxB) signals, peptide influx (R12), and membrane particle formation (DIC). Time 0: images captured immediately before the addition of the arginine peptides. (**c**) Immunofluorescence staining with lysenin, a sphingomyelin-specific probe. The localization of lysenin in HeLa cells incubated with R12-Alexa488 (5 μmol/l) for 5 minutes at 37 °C or 4 °C is shown. Arrows indicate sites of membrane particles. Bar = 20 μm. DIC, differential interference contrast.

Since sialic glycolipids have been suggested to be abundant in lipid raft microdomains,[18] we studied the possible involvement of lipid raft microdomains in particle formation. Lipid raft microdomains have been reported to be rich in cholesterol and sphingomyelin (SM).[19] We used the SM-specific probe lysenin[20] to monitor the localization of SM in cells incubated with R12-Alexa488 (Figure 3c). Treatment of cells with R12-Alexa488 led to significant SM accumulation at the sites of membrane particles (compare the three horizontal panels (arrows) in Figure 3c), suggesting a role for microdomains in particle formation. However, the formation of membrane particles and accumulation of SM were also observed when cells were also treated with MβCD, a reagent that extracts cholesterol from cell membranes and thereby disrupts lipid raft/caveolae microdomains (**Supplementary Figure S6**). This suggests that lipid raft/caveolae microdomains may not be indispensable for particle formation.

Membrane particles were formed at 4 °C, but SM did not accumulate at the sites of particle formation at this temperature (Figure 3c). This indicates that the lipid composition of the membrane particles may be different at 4 °C and 37 °C, perhaps because of a decrease in the lateral diffusion of membrane lipids at 4 °C. Therefore, the mechanisms by which the particles are formed at 4 °C and 37 °C may not be identical.

Structural analysis of membrane particles by electron microscopy

To obtain more information about the detailed structures of the membrane particles formed following peptide treatment, electron microscopic analysis was conducted. For electron microscopy, fixation procedure of samples with, for example, 2% glutaraldehyde, is usually necessary before osmium tetroxide treatment and dehydration. However, artifacts in the cellular localization of arginine-rich peptides caused by fixation have been noted.[9] Therefore, we carefully reassessed the effects of fixation on the cellular localization and on internalization of the R12 peptide using acetone/methanol (1:1), 4% paraformaldehyde (PFA), and 2% glutaraldehyde (GA) as fixation reagents (**Supplementary Figure S7**). We found no significant artifacts in the cellular localization of R12-Alexa488 when using either 4% paraformaldehyde or 2% GA, as long as we avoided using mounting media for microscopic observation. When we used 2% GA under conditions allowing both endocytic uptake and direct diffusion into the cytosol, signals for R12-Alexa488 were particularly well retained, even after fixation (**Supplementary Figure S7**). Two percent GA in 30 mmol/l 4-(2-hydroxyethyl)-1-piperazineethanesulfonic acid (HEPES) is a standard solution for primary fixation when performing electron microscopic analysis. We thus obtained electron micrographs of cells treated

with R12-Alexa488 after 2% GA fixation followed by osmium tetroxide treatment and dehydration (Figure 4).

Detailed structures of the membrane particles formed after treatment with R12-Alexa488 were clearly observed by scanning electron microscopy. Unexpectedly, the magnified images of these particles revealed that they did not have a simple large vesicular structure, but instead consisted of many small vesicles of various diameters (~50–500 nm) (Figure 4a). In addition, smaller, presumably "immature" particles consisting of one or a few vesicles were observed throughout the membranes of peptide-treated cells, whereas no such vesicles were detected in control cells (Figure 4b). This suggests that treatment with R12-Alexa488 induces the formation of these vesicles on plasma membranes and that their eventual accumulation results in formation of the large particles identified by confocal microscopy as the sites of peptide influx. The vesicle-stacking structures of these particles were further studied by transmission electron microscopy (TEM). Analysis of vertical sections of peptide-treated cells revealed the complex structures of the particles (Figure 4c). The vesicles from which the membrane particles were formed consisted of multilamellar lipid membranes, each with an internal hollow space (Figure 4c). Significant formation of particle structures was not observed in the cells that were not treated with the peptide (Figure 4d).

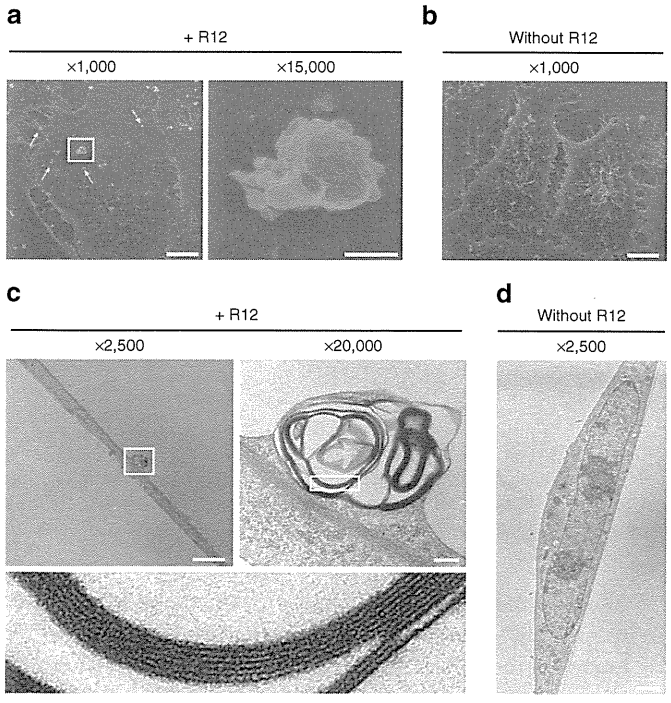

Figure 4 Electron microscopic analysis showing that the membrane particles formed following R12-Alexa488 treatment consist of multiple multilamellar vesicles stacked on top of each other. (**a**,**b**) HeLa cells were treated (**a**) with or (**b**) without R12-Alexa488 (6 μmol/l) in α-MEM(–) for 5 minutes, fixed through incubation with 2% glutaraldehyde in 30 mmol/l HEPES, and then analyzed by SEM. The right image in **a** is a magnified image of the membrane particle highlighted in the left image. Arrows indicate single vesicles or immature particles composed of small numbers of vesicles. (**c**,**d**) Cells were treated (**c**) with or (**d**) without R12-Alexa488 as in **a**,**b** and analyzed by TEM. The upper-right image in **c** is a magnified image of the membrane particle highlighted in the upper-left image, and the lower image in **c** is a magnified image of the highlighted region in the upper-right image. Bars = 10 μm (**a**, left; **b**), 1 μm (**a**, right), 2 μm (**c**, left; **d**), and 200 nm (**c**, right). HEPES, 4-(2-hydroxyethyl)-1-piperazineethanesulfonic acid; SEM, scanning electron microscopy; TEM, transmission electron microscopy.

Live-CLEM

To obtain more detailed information on the formation of membrane particles, we analyzed cells treated with R12-Alexa488 using correlative light and electron microscopy after live-cell imaging (Live-CLEM) (Figure 5 and **Supplementary Figure S8**).[21] This method, recently developed by Haraguchi and coworkers, is a powerful tool for monitoring TEM images of the same cells that were observed by time-lapse live imaging. We used it in an effort to confirm that the multilamellar vesicle structures described above were actually formed at the sites of peptide influx as a function of time. Live-cell imaging of HeLa cells treated with 5 μmol/l R12-Alexa488 was carried out at 37 °C using a confocal microscope. The cells were then fixed with GA 1 minute after membrane particles were observed (~2 minutes after addition of the peptide) (arrows in Figure 5a and **Supplementary Figure S8**). The fixed cells were then subjected to TEM, which revealed the formation of multilamellar membrane structures a short time after treatment of the cells with the peptide (Figure 5). Z-stack analysis of the TEM images revealed that the distribution of the multilamellar structures ranged from sections 1–10 (counting from the bottom to the top in 80-nm intervals) (Figure 5d). While the lower part of the particle (sections 1–6) was buried inside the cells, membrane structures extruding from the cell surface were also observed for the upper sections (7–10). Analysis of representative membrane particles suggested that their diameters and heights were in the ranges 0.5–1 μm and 2–3 μm, respectively. Similar membrane structures were also observed in cells treated with R12-Alexa488 at 4 °C (**Supplementary Figure S9**), suggesting that the structural alterations in plasma membranes were induced by an energy-independent, physicochemical interaction between R12-Alexa488 and the plasma membrane.

Importance of the attachment of hydrophobic moieties to the R12 peptide for membrane-particle formation

To assess the possible contribution of the fluorescent moiety to particle formation, we analyzed whether non-labeled R12 also triggered the formation of particle-like structures. Although particle structures were formed within 6 minutes after treatment with 5 μmol/l R12-Alexa488 (Figure 6), very few were observed after treatment with non-fluorescently labeled R12, even after treatment at a higher concentration (20 μnol/l) for several minutes (Figure 6 and **Supplementary Figure S10a**). The application of non-labeled R12 at a concentration of 100 μmol/l yielded fewer particle-like structures within 8–10 minutes than treatment with 5 μmol/l R12-Alexa488 (**Supplementary Figure S10b**). These results suggest the potential contribution of the Alexa Fluor 488 moiety to particle formation. Considering the effect of Alexa Fluor 488 as a source of hydrophobicity, we next examined whether the attachment of other hydrophobic moieties also contributed to the ability of the peptide to induce particle formation. HAtag (YPYDVPDYA) is a short, relatively hydrophobic peptide that is used for protein and peptide detection via immunostaining and

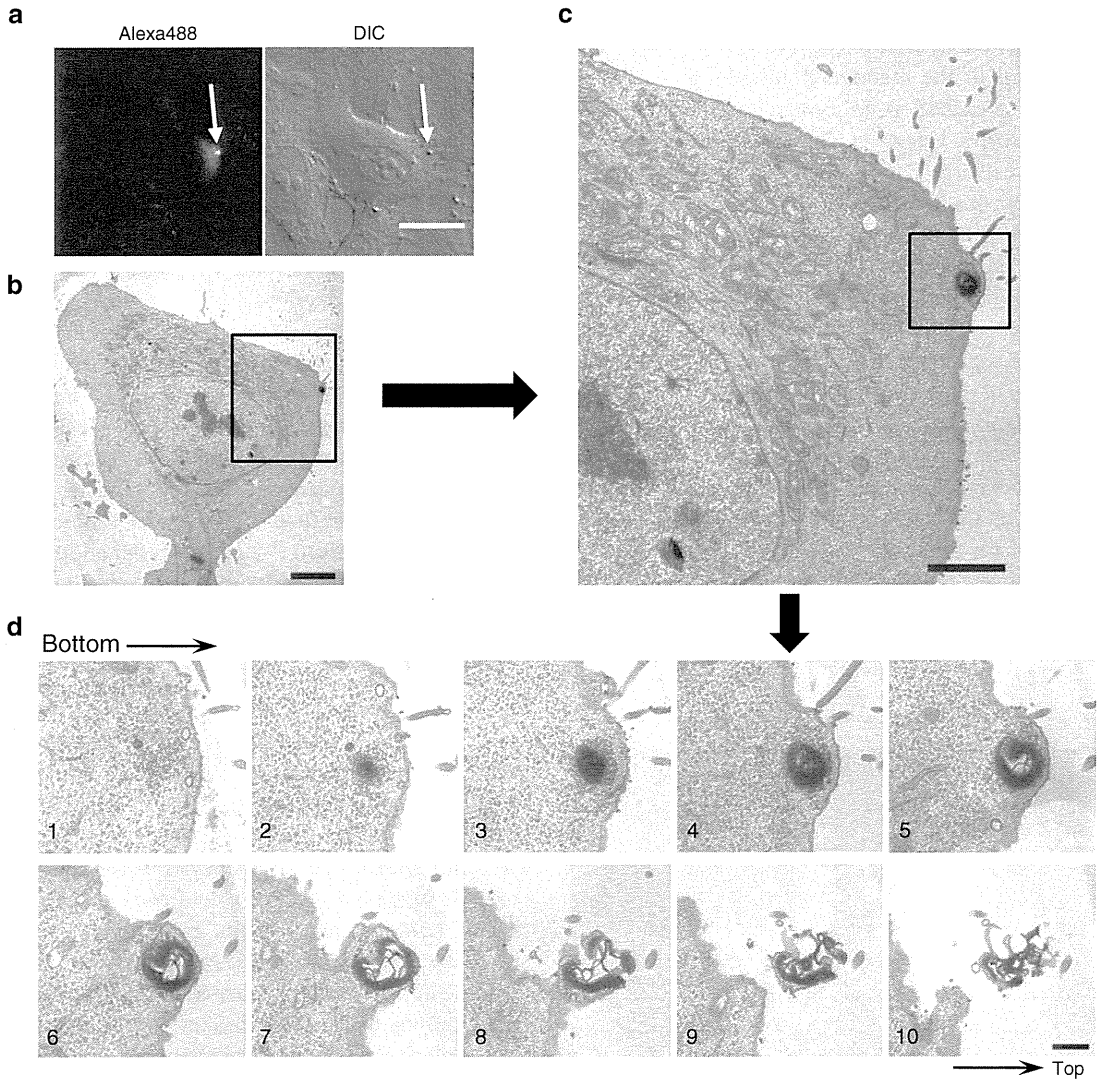

Figure 5 Correlative light and electron microscopy after live-cell imaging (Live-CLEM) of cells treated with R12-Alexa488. (**a**) HeLa cells were treated with R12-Alexa488 (5 μmol/l) in α-MEM(–) for 3 minutes (left, fluorescence image; right, DIC image). Bar = 20 μm. (**b**) Electron microscopic image of the cell identified with an arrow in **a**. Bar = 5 μm. (**c**) Enlarged image of the highlighted image in **b**. Bar = 2 μm. (**d**) Z-stack electron microscopic analysis of the highlighted area in **c**. Intervals = 80 nm. Bar = 500 nm. CLEM, correlative light and electron microscopy; DIC, differential interference contrast; MEM, minimum essential medium.

western blotting. We synthesized a hybrid peptide comprising R12 and HAtag sequences (R12-HAtag).

We next examined whether particles formed on the surfaces of HeLa cells following treatment with the R12-HAtag peptide. As expected, significant particle formation was observed following the treatment of cells with 20 μmol/l R12-HAtag (Figure 6). Particle formation accompanied direct peptide penetration through plasma membranes after treatment of HeLa cells with fluorescein-labeled R12 (R12-fluorescein) (**Supplementary Figure S10c**). In addition, we previously reported direct penetration of octa-arginine bearing a hexanoyl moiety on its N-terminus through plasma membranes,[22] which was also accompanied by membrane-particle formation (**Supplementary Figure S10d**). These results suggest that the attachment of an appropriate hydrophobic moiety to the R12 peptide or other arginine-rich peptides stimulates the formation of membrane particles on the cell surface, and this may have a strong correlation with the influx of peptide into cells.

Even modified with hydrophobic moieties, the R12 peptide seems unlikely to form aggregates or micelles in culture media. We examined the critical micelle concentration using R12-HAtag. Micelle/aggregate formation of the peptide should yield increases in the fluorescence intensity of the environment-sensitive fluorescence additive 1,6-diphenyl-1,3,5-hexatriene (DPH).[23] However, no significant increase in fluorescence intensity was observed, even after treatment with 6 mg/ml (*i.e.*, ~2 mmol/l) R12-HAtag (**Supplementary Figure S11**).

Assessment of plasma membrane integrity and involvement of membrane-repair mechanisms

Plasma membrane integrity upon membrane-particle formation was then confirmed by the lactate dehydrogenase-release assay, as reported previously.[16] The lack of significant leakage of lactate dehydrogenase from cells incubated with R12-HAtag for 30 minutes in phosphate-buffered saline (+) indicated integrity

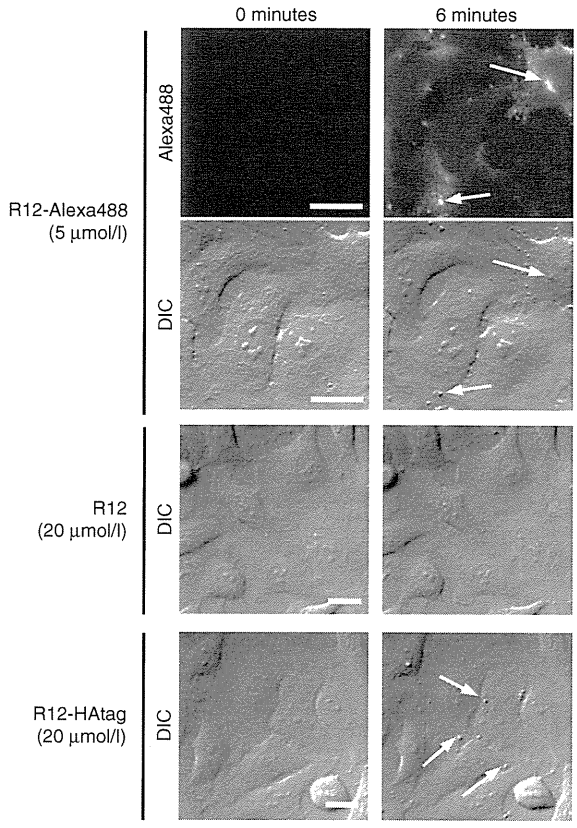

Figure 6 Importance of the hydrophobic moiety to the formation of particle structures. Time-lapse observation of HeLa cells incubated with R12-Alexa488 (5 μmol/l), R12 (20 μmol/l), or R12-HAtag (20 μmol/l). Time 0: images captured immediately before the addition of the arginine peptides. Arrows indicate membrane particles. Bar = 20 μm. DIC, differential interference contrast.

of the peptide-treated plasma membranes (**Supplementary Figure S12**).

Palm-Apergi *et al.* reported the induction of membrane-repair responses in cells treated with a model amphipathic peptide and penetratin.[24] These CPPs have basic and amphipathic structures. Thus, we examined whether the direct peptide influx through plasma membranes and membrane-particle formation were accompanied by a membrane-repair response. There are several membrane-repair systems, and one of the most studied of these mechanisms is mediated by exocytosis of lysosomes or endosomes.[25] If the lysosome-mediated membrane-repair response is induced at the location of membrane-particle formation, lysosomal proteins should be exposed on the cell membranes, and the recruitment of lysosomal-associated membrane protein 2 (LAMP-2) to these regions should be observed.[24] However, LAMP-2 was not detected near these particles (**Supplementary Figure S13a**). We also examined the internalization of R12-Alexa488 in the presence of 10 mmol/l dithiothreitol (DTT). It has been reported that oxidative conditions are necessary for the membrane-repair machinery that uses MG53, and this membrane-repair system does not work in the presence of reducing agents such as DTT.[26] Membrane-particle formation accompanied R12-Alexa488 influx in the presence of DTT, suggesting that this oxidative repair system was not involved (**Supplementary Figure S13b**).

Further studies are required to determine the involvement of other membrane-repair systems to membrane-particle formation. However, our results indicate that the formation of membrane particles is not due to lysosome- or endosome-mediated membrane-repair responses.

Translocation of R12-Alexa488 into giant vesicles

To examine whether the formation of membrane particles can be solely explained by the interaction of membrane lipids with arginine-rich peptides, the influx of R12-Alexa488 was studied using giant vesicles (GVs) that mimic the composition of plasma membranes (27.5% 1,2-dioleoyl-*sn*-glycero-3-phosphocholine (DOPC), 12.2% 1,2-dioleoyl-*sn*-glycero-3-phospho-L-serine (DOPS), 17.0% 1,2-dioleoyl-*sn*-glycero-3-phosphoethanolamine (DOPE), 8.8% SM, and 34.5% cholesterol (Chol) (in mol%))[27] (**Supplementary Figure S14**). As membrane potential should play a crucial role in the translocation of the R12 peptide through membranes, liposomes were formed using a K^+-rich buffer (50 mmol/l K_2SO_4, 10 mmol/l Tris-HCl, and 200 mmol/l sucrose, pH 7.4) for the inside of the liposomes and a Na^+-rich buffer (50 mmol/l Na_2SO_4, 10 mmol/l Tris-HCl, and 200 mmol/l sucrose, pH 7.4) as the outside buffer, followed by the addition of valinomycin as a potassium-selective ionophore. These conditions led to translocation of potassium ions through the membranes to the outside of the GVs, with no permeation by sodium ions, yielding inside-negative membrane potentials. Although no significant translocation of R12-Alexa488 (2.5 μmol/l, peptide:lipid ratio = 1:10) was observed in the GVs in the absence of valinomycin treatment (**Supplementary Figure S14c**), influx of R12-Alexa488 was observed in ~30% of the valinomycin-treated GVs (**Supplementary Figure S14d**). Gramicidin A is a peptide ion channel that transports both potassium and sodium ions. Treatment of the GVs with gramicidin A yielded no membrane potential and no peptide translocation (data not shown). These results highlighted the importance of membrane potential for the translocation of arginine-rich peptide through membranes.

Particle-like lipid domains that accumulated peptide were observed on the liposomal membrane (arrows in **Supplementary Figure S14c,d**). However, similar structures were also found on the liposomes before treatment with R12-Alexa488 (arrow in **Supplementary Figure S14a**), suggesting that these lipid structures were not formed by interaction with R12-Alexa488. It is possible that the penetration of peptide into living cells occurs through peptide–lipid interactions in the presence of a membrane potential. However, other cellular components, including membrane proteins, sugar chains, or cytosolic proteins, would also be necessary for the formation of membrane particles.

Influx of R4-Alexa488 into cells treated with R12-HAtag

The influx of R12 peptides bearing hydrophobic moieties may lead to membrane particle formation. This may be accompanied by local and transient alterations in the lipid bilayer structure. Coincubation with an R12 peptide bearing a hydrophobic moiety may also promote the translocation of peptides with low membrane permeability. To examine this hypothesis, R4-Alexa488 was employed as a model molecule with limited membrane permeability.[6]

HeLa cells were treated with R4-Alexa488 (10 μmol/l) in the presence of non-labeled R4-, R12-, and R12-HAtag peptides. As expected, a marked increase in the cellular uptake of R4-Alexa488 was observed in the presence of 20 μmol/l R12-HAtag (Figure 7a, rightmost column). Efficient influx of R4-Alexa488 and membrane-particle formation were also observed by confocal microscopy (Figure 7b, bottom right panels). In contrast, only a slight increase in the cellular uptake of R4-Alexa488 (10 μmol/l) was observed in cells that were cotreated with non-labeled R12 (20 or 100 μmol/l) (Figure 7a, middle column), even though confocal microscopic observation showed diffuse signals for R4-Alexa488 (Figure 7b, upper-right panels). Addition of non-labeled R4 (60 μmol/l) did not significantly increase the cellular uptake of R4-Alexa488.

Note that when GC-Alexa488, which contains no arginine residues, was applied at a concentration of 10 μmol/l in the presence of 20 μmol/l R12-HAtag, a significant influx of GC-Alexa488 into cells occurred, although the influx was weaker than that observed with R4-Alexa488 (Figure 7c, right).

The above results suggest that (i) R12 peptides bearing hydrophobic moieties have a much greater ability to directly penetrate into cells through the plasma membrane; (ii) membrane-particle formation may accompany the influx of peptides into cells; and (iii) the influx of R12-HAtag may lead to transient structural alterations in membrane lipid bilayers that allow the translocation of R4-Alexa488 and GC-Alexa488, which are otherwise unable to permeate the plasma membrane.

DISCUSSION

The careful live-cell observations performed in this study clearly revealed that direct internalization of R12-Alexa488 is accompanied by several events, including the formation of concentrated peptide regions and membrane particles, together with membrane inversion and the accumulation of negatively charged membrane components in the vicinity of the influx sites. In addition, electron microscopic analysis revealed the detailed structures of the membrane particles, which consisted of small vesicles stacked on top of each other. The interaction of R12-Alexa488 with the plasma membrane induced dynamic alterations in plasma membrane structures that led to the direct influx of the peptide. In addition, we showed that the conjugation of R12 to Alexa Fluor 488 or HAtag was important for the formation of the particles, which strongly suggests that the hydrophobic properties of the conjugated moiety may be important for accelerating R12 peptide-dependent penetration into the cell. The addition of hydrophobic moieties to the R12 peptide may increase its amphiphilicity or detergent-like activity. However, considering that the direct internalization of these peptides is not accompanied by apparent membrane impairment, the mechanisms of translocation of R12 conjugated

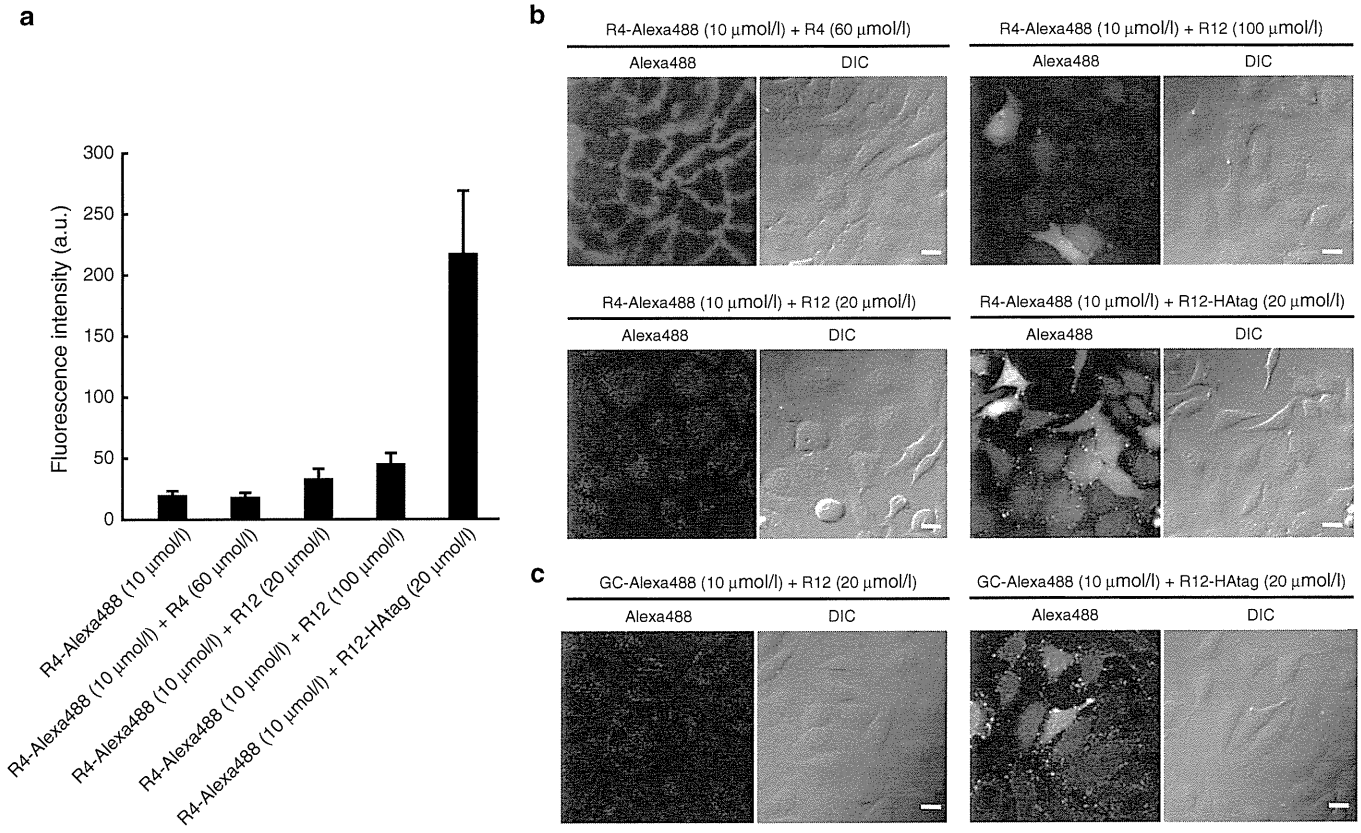

Figure 7 Coincubation with R12-HAtag stimulated the internalization of R4-Alexa488. (**a**) FACS analysis of the cellular uptake of R4-Alexa488 (10 μmol/l) in the presence or absence of R4 (60 μmol/l), R12 (20 μmol/l or 100 μmol/l), or R12-HAtag (20 μmol/l). Treatment at 37 °C for 10 minutes. Data show the mean ± SD (n = 3). (**b**) Confocal microscopic analysis of the cellular uptake of R4-Alexa488 in the presence of R4 (60 μmol/l), R12 (20 μmol/l or 100 μmol/l), or R12-HAtag (20 μmol/l). (**c**) Confocal microscopic analysis of the cellular uptake of GC-Alexa488 in the presence of R12 (20 μmol/l) or R12-HAtag (20 μmol/l). Bar = 20 μm. a.u., arbitrary unit; DIC, differential interference contrast; FACS, fluorescence-activated cell sorting.

to Alexa Fluor 488 or HAtag cannot be explained by simple membrane perturbation or transient pore formation, as was observed for cationic amphiphilic antimicrobial peptides.[28]

We and others have previously reported the direct flux of oligoarginine peptides through specific points on the plasma membrane in the absence of serum or at relatively high peptide concentrations.[14,16] However, the formation of unique particle structures associated with the sites of peptide influx is novel to this study. Note that the particles do not possess the simple bleb-like structure of outwardly expanding plasma membranes,[29] but have a complex yet unique structure formed from multiple vesicles with multilamellar membranes. Ziegler *et al.* reported the formation of dense aggregates on the surfaces of fibroblast cells treated with the Tat peptide.[30] However, the aggregates were different in size and shape from the particles observed in this study.

Although the mechanism by which these particle-like structures are formed remains unclear at present, cellular components other than lipids are likely involved in morphological alterations of the plasma membrane and consequent peptide influx into the cytosol. Membrane-associated negatively charged molecules such as sialic acids may also be directly or indirectly involved in this process because those molecules can form complexes with oligoarginine peptides through electrostatic interactions. The absence of obvious particle-like structures after addition of R12 to GVs further supported our assumption that membrane-particle formation in living cells is not due to the simple interaction of the peptides with lipids. Obviously, further analysis is required to identify the cellular components responsible for interactions with, and structural alterations of, the plasma membrane.

The formation of the membrane particles may be highly dependent on the number of arginine residues in the peptide. The R12 peptide has a stronger affinity for the plasma membrane than the R8 and R4 peptides and more strongly induces direct influx. Conjugation of a hydrophobic segment to the R12 peptide may further increase the interaction of the peptide to the plasma membrane and thereby induce direct influx of the peptide and the formation of the unique particle-like membrane structures. The formation of multilamellar membrane structures strongly suggests the involvement of membrane fusion or hemifusion in this process. Increasing the amphiphilicity of the R12 peptides through the attachment of a hydrophobic segment and the potential ability of arginine-rich CPPs to induce curvature in the membrane[31–34] may also play roles in the formation of the unique membrane structures.

Strong fluorescent signals of Alexa-labeled R12 peptide observed inside the membrane particles suggested the entrapment of the R12 peptide in the multilamellar structure. It is unclear whether the peptide penetrated through the multilamellar structures to enter the cells. However, the peptides likely form complexes with other membrane-associated molecules in the particles, and it would be inefficient to translocate through multiple membranes while dissociating from these molecules. Alternatively, peptide influx into cells may lead to local perturbation of the membrane structures to yield particle-like structures. Peptide influx may also lead to phase separation of the membranes by the recruitment of GM1 and SM to the sites of peptide internalization, as observed in this study. Consistent with this, the direct penetration of nona-arginine (R9) was recently reported to induce the translocation of acid SMase to the outer leaflet of the plasma membrane and, subsequently, ceramide formation.[35] The induction of phase separation upon particle formation may accelerate the influx of peptides into cells through the membranes.[36]

The results obtained in this study provide novel insights from the perspective of drug delivery. First, the attachment of Alexa Fluor 488 or HAtag significantly enhanced membrane-particle formation. This should shed light on ways of optimizing R12 as an intracellular delivery vector because direct penetration of R12 can be accelerated by the attachment of hydrophobic cargo compounds of relatively low molecular weights. Second, with the help of R12-HAtag, molecules with low membrane permeability (R4-Alexa488 and GC-Alexa488) were successfully delivered to the cytosol. The dynamic structural alterations in the plasma membrane induced by R12-HAtag may allow synchronized translocation of these molecules into cells, while the affinity of the conjugate for the cell surface may be an important factor determining the efficacy of translocation.

In summary, through the above studies on the mechanisms of direct internalization of the R12 peptide, we have identified novel properties of oligoarginine peptides that induce unique multimeric particle formation. The above results should have an impact on the design of novel intracellular delivery systems for low-molecular-weight compounds that cannot permeate the cell membrane.

MATERIALS AND METHODS

Peptides. All the peptides used in this study were chemically synthesized and fluorescently labeled using Alexa 488 or Alexa568 C_5 maleimide sodium salt (Invitrogen, Carlsbad, CA) or 5-(Iodoacetamido)fluorescein (Sigma, St Louis, MO) as already reported.[13] The actual sequences of the synthesized peptides are as follows: R12, NH_2-$(Arg)_{12}$-amide; R12-Alexa488, NH_2-$(Arg)_{12}$-Gly-Cys(Alexa488)-amide; R12-HAtag, NH_2-$(Arg)_{12}$-$(Gly)_2$-Tyr-Pro-Tyr-Asp-Val-Pro-Asp-Tyr-Ala-amide; R4, NH_2-$(Arg)_4$-amide; R4-Alexa488, NH_2-$(Arg)_4$-Gly-Cys(Alexa488)-amide; GC-Alexa488, NH_2-Gly-Cys(Alexa488)-amide; R12-fluorescein, NH_2-$(Arg)_{12}$-Gly-Cys(fluorescein)-amide; R12-Alexa568, NH_2-$(Arg)_{12}$-Gly-Cys(Alexa568)-amide; Hexanoyl R8-Alexa, $C_5H_{11}CO$-$(Arg)_8$-Gly-Cys(Alexa488)-amide.

Correlative light and electron microscopy after live-cell imaging (Live-CLEM). HeLa cells were cultured on a grid-based, glass-bottomed culture dish (Iwaki, Chiba, Japan). The cells were washed with α-minimum essential medium (MEM)(−) twice, incubated with 150 μl of α-MEM(−), and allowed to settle for 10 minutes in an MI-IBC microchamber attached to the stage of an inverted microscope. The incubator provided a humidified atmosphere containing 5% CO_2 and a temperature of 37 °C. Next, R12-Alexa488 (final concentration, 5 μmol/l) was added to the cells and time-lapse imaging was carried out. Glutaraldehyde (final concentration 2.5%) was added to the medium at the desired time point (1, 2, or 5 minutes) after membrane particles were observed, and the cells were allowed to settle before fixation. After washing three times with phosphate-buffered saline, three-dimensional images of the same cells (at 0.2-μm intervals) were acquired using a confocal microscope equipped with a 60× objective lens (oil, NA 1.35).

TEM analysis of the same cells observed by confocal microscopy was conducted as described previously.[21] Briefly, cells were postfixed with 1% OsO_4 (cat. no. 3002; Nisshin EM, Tokyo, Japan). After partial dehydration through incubation in 30% ethanol for 1 minute, 50% ethanol for 3 minutes, and 70% ethanol for 5 minutes, the cells were stained with 2% uranyl acetate (cat. no. 554-85072; Wako Pure Chemical Industries, Osaka, Japan) in 70% ethanol for 30 minutes, and then completely dehydrated through incubation in 90% ethanol for 5 minutes and 100% ethanol for 5 minutes. The cells were then embedded in epoxy resin through incubation with 10, 30, 50, 70, and 90% (vol/vol) Epon812 (cat. no. T024; TAAB

Laboratories Equipment, Berkshire, UK) in ethanol and 100% Epon812. The epoxy block containing the same cells that had been observed by confocal microscopy was trimmed according to the grid address on the glass base, and sectioned using an ultramicrotome (Leica Microsystems, Wetzlar, Germany), yielding ultrathin sections with a thickness of 80 nm. These sections were stained with 4% uranyl acetate for 15 minutes and a commercial ready-to-use solution of lead citrate (cat. no. 18-0875-2; Sigma) for 1 minute. Images were acquired using a JEM-2000EX electron microscope (80 kV; JEOL, Tokyo, Japan).

Details of the other experiments performed are provided in the **Supplementary Materials and Methods**.

SUPPLEMENTARY MATERIAL

Figure S1. Direct internalization of R12-Alexa488 into the cytosol, initiated at a site on the plasma membrane with an intense fluorescent signal.

Figure S2. The R12-Alexa488 spots strongly colocalize with transiently formed membrane particles.

Figure S3. Time-lapse images of cells incubated with R12-Alexa488 at 15°C and R4-Alexa488 at 37°C.

Figure S4. The effect of macropinocytosis inhibitors on the formation of membrane particles.

Figure S5. Effect of membrane potential on particle formation and influx of R12-Alexa488 into cells.

Figure S6. Immunofluorescence staining of MβCD-treated and control cells with lysenin.

Figure S7. Effects of fixation procedures on the internalization of R12-Alexa488 and cellular morphology.

Figure S8. Live-cell imaging for correlative light and electron microscopy (CLEM) (see also Figure 5).

Figure S9. Correlative light and electron microscopy (CLEM) of cells treated with R12-Alexa488 for 1 minute at 4 °C.

Figure S10. Treatment of HeLa cells with nonlabeled R12, R12-fluorescein, and Hexanoyl R8-Alexa488.

Figure S11. Analysis of critical micelle concentration (CMC).

Figure S12. Assessment of plasma membrane integrity by LDH release assay.

Figure S13. Examination of plasma membrane-repair responses.

Figure S14. R12-Alexa488 translocation into GVs that mimic plasma membranes with membrane potential.

Video S1. Time-lapse images of the cells incubated with R12-Alexa488 (5 μmol/l) that correspond to Figure S1.

Materials and Methods

ACKNOWLEDGMENTS

This work was supported in part by Grants-in-Aid for Scientific Research from the Ministry of Education, Culture, Sports, Science and Technology of Japan to I.N., S.K., T.H., and S.F. T.T. and H.H. are grateful for a JSPS Research Fellowship for Young Scientists and S.P. is grateful for a JSPS Postdoctoral Fellowship for Foreign Researchers. The authors are grateful to Takamasa Hanaichi for his technical assistant with the electron microscopic observations for Figure 4. The authors declared no conflict of interest.

REFERENCES

1. Joliot, A and Prochiantz, A (2004). Transduction peptides: from technology to physiology. *Nat Cell Biol* **6**: 189–196.
2. Futaki, S (2008). Membrane permeable peptide vectors: chemistry and functional design for the therapeutic applications. *Adv Drug Deliv Rev* **60**: 447.
3. Futaki, S, Suzuki, T, Ohashi, W, Yagami, T, Tanaka, S, Ueda, K *et al.* (2001). Arginine-rich peptides. An abundant source of membrane-permeable peptides having potential as carriers for intracellular protein delivery. *J Biol Chem* **276**: 5836–5840.
4. Rothbard, JB, Garlington, S, Lin, Q, Kirschberg, T, Kreider, E, McGrane, PL *et al.* (2000). Conjugation of arginine oligomers to cyclosporin A facilitates topical delivery and inhibition of inflammation. *Nat Med* **6**: 1253–1257.
5. Vivès, E, Brodin, P and Lebleu, B (1997). A truncated HIV-1 Tat protein basic domain rapidly translocates through the plasma membrane and accumulates in the cell nucleus. *J Biol Chem* **272**: 16010–16017.
6. Nakase, I, Takeuchi, T, Tanaka, G and Futaki, S (2008). Methodological and cellular aspects that govern the internalization mechanisms of arginine-rich cell-penetrating peptides. *Adv Drug Deliv Rev* **60**: 598–607.
7. Wender, PA, Galliher, WC, Goun, EA, Jones, LR and Pillow, TH (2008). The design of guanidinium-rich transporters and their internalization mechanisms. *Adv Drug Deliv Rev* **60**: 452–472.
8. Snyder, EL and Dowdy, SF (2005). Recent advances in the use of protein transduction domains for the delivery of peptides, proteins and nucleic acids in vivo. *Expert Opin Drug Deliv* **2**: 43–51.
9. Richard, JP, Melikov, K, Vives, E, Ramos, C, Verbeure, B, Gait, MJ *et al.* (2003). Cell-penetrating peptides. A reevaluation of the mechanism of cellular uptake. *J Biol Chem* **278**: 585–590.
10. Jones, AT (2007). Macropinocytosis: searching for an endocytic identity and role in the uptake of cell penetrating peptides. *J Cell Mol Med* **11**: 670–684.
11. Nakase, I, Niwa, M, Takeuchi, T, Sonomura, K, Kawabata, N, Koike, Y *et al.* (2004). Cellular uptake of arginine-rich peptides: roles for macropinocytosis and actin rearrangement. *Mol Ther* **10**: 1011–1022.
12. Wadia, JS, Stan, RV and Dowdy, SF (2004). Transducible TAT-HA fusogenic peptide enhances escape of TAT-fusion proteins after lipid raft macropinocytosis. *Nat Med* **10**: 310–315.
13. Nakase, I, Tadokoro, A, Kawabata, N, Takeuchi, T, Katoh, H, Hiramoto, K *et al.* (2007). Interaction of arginine-rich peptides with membrane-associated proteoglycans is crucial for induction of actin organization and macropinocytosis. *Biochemistry* **46**: 492–501.
14. Duchardt, F, Fotin-Mleczek, M, Schwarz, H, Fischer, R and Brock, R (2007). A comprehensive model for the cellular uptake of cationic cell-penetrating peptides. *Traffic* **8**: 848–866.
15. Fretz, MM, Penning, NA, Al-Taei, S, Futaki, S, Takeuchi, T, Nakase, I *et al.* (2007). Temperature-, concentration- and cholesterol-dependent translocation of L- and D-octa-arginine across the plasma and nuclear membrane of CD34+ leukaemia cells. *Biochem J* **403**: 335–342.
16. Kosuge, M, Takeuchi, T, Nakase, I, Jones, AT and Futaki, S (2008). Cellular internalization and distribution of arginine-rich peptides as a function of extracellular peptide concentration, serum, and plasma membrane associated proteoglycans. *Bioconjug Chem* **19**: 656–664.
17. Koivusalo, M, Welch, C, Hayashi, H, Scott, CC, Kim, M, Alexander, T *et al.* (2010). Amiloride inhibits macropinocytosis by lowering submembranous pH and preventing Rac1 and Cdc42 signaling. *J Cell Biol* **188**: 547–563.
18. Matsuzaki, K, Noguch, T, Wakabayashi, M, Ikeda, K, Okada, T, Ohashi, Y *et al.* (2007). Inhibitors of amyloid beta-protein aggregation mediated by GM1-containing raft-like membranes. *Biochim Biophys Acta* **1768**: 122–130.
19. Simons, K and Ikonen, E (1997). Functional rafts in cell membranes. *Nature* **387**: 569–572.
20. Yamaji, A, Sekizawa, Y, Emoto, K, Sakuraba, H, Inoue, K, Kobayashi, H *et al.* (1998). Lysenin, a novel sphingomyelin-specific binding protein. *J Biol Chem* **273**: 5300–5306.
21. Haraguchi, T, Kojidani, T, Koujin, T, Shimi, T, Osakada, H, Mori, C *et al.* (2008). Live cell imaging and electron microscopy reveal dynamic processes of BAF-directed nuclear envelope assembly. *J Cell Sci* **121**: 2540–2554.
22. Katayama, S, Hirose, H, Takayama, K, Nakase, I and Futaki, S (2011). Acylation of octaarginine: Implication to the use of intracellular delivery vectors. *J Control Release* **149**: 29–35.
23. Ryu, DW, Kim, HA, Song, H, Kim, S and Lee, M (2011). Amphiphilic peptides with arginines and valines for the delivery of plasmid DNA. *J Cell Biochem* **112**: 1458–1466.
24. Palm-Apergi, C, Lorents, A, Padari, K, Pooga, M and Hällbrink, M (2009). The membrane repair response masks membrane disturbances caused by cell-penetrating peptide uptake. *FASEB J* **23**: 214–223.
25. McNeil, PL and Steinhardt, RA (2003). Plasma membrane disruption: repair, prevention, adaptation. *Annu Rev Cell Dev Biol* **19**: 697–731.
26. Cai, C, Masumiya, H, Weisleder, N, Matsuda, N, Nishi, M, Hwang, M *et al.* (2009). MG53 nucleates assembly of cell membrane repair machinery. *Nat Cell Biol* **11**: 56–64.
27. D'Antuono, C, Fernández-Tomé, MC, Sterin-Speziale, N and Bernik, DL (2000). Lipid-protein interactions in rat renal subcellular membranes: a biophysical and biochemical study. *Arch Biochem Biophys* **382**: 39–47.
28. Matsuzaki, K, Nakamura, A, Murase, O, Sugishita, K, Fujii, N and Miyajima, K (1997). Modulation of magainin 2-lipid bilayer interactions by peptide charge. *Biochemistry* **36**: 2104–2111.
29. Tournaviti, S, Hannemann, S, Terjung, S, Kitzing, TM, Stegmayer, C, Ritzerfeld, J *et al.* (2007). SH4-domain-induced plasma membrane dynamization promotes bleb-associated cell motility. *J Cell Sci* **120**: 3820–3829.
30. Ziegler, A, Nervi, P, Dürrenberger, M and Seelig, J (2005). The cationic cell-penetrating peptide CPP(TAT) derived from the HIV-1 protein TAT is rapidly transported into living fibroblasts: optical, biophysical, and metabolic evidence. *Biochemistry* **44**: 138–148.
31. Lamazière, A, Wolf, C, Lambert, O, Chassaing, G, Trugnan, G and Ayala-Sanmartin, J (2008). The homeodomain derived peptide Penetratin induces curvature of fluid membrane domains. *PLoS ONE* **3**: e1938.
32. Afonin, S, Frey, A, Bayerl, S, Fischer, D, Wadhwani, P, Weinkauf, S *et al.* (2006). The cell-penetrating peptide TAT(48-60) induces a non-lamellar phase in DMPC membranes. *Chemphyschem* **7**: 2134–2142.
33. Mishra, A, Gordon, VD, Yang, L, Coridan, R and Wong, GC (2008). HIV TAT forms pores in membranes by inducing saddle-splay curvature: potential role of bidentate hydrogen bonding. *Angew Chem Int Ed Engl* **47**: 2986–2989.
34. Sakamoto, K, Takino, Y and Ogasawara, K. Methods for controlling membrane permeability of a membrane permeable substance and screening methods for a membrane permeable substance. In: USP appl 2005/0118204, 2 Jun 2005 (JP appl 2003-3774224, 4 Nov 2003).
35. Verdurmen, WP, Thanos, M, Ruttekolk, IR, Gulbins, E and Brock, R (2010). Cationic cell-penetrating peptides induce ceramide formation via acid sphingomyelinase: implications for uptake. *J Control Release* **147**: 171–179.
36. Montes, LR, Ruiz-Argüello, MB, Goñi, FM and Alonso, A (2002). Membrane restructuring via ceramide results in enhanced solute efflux. *J Biol Chem* **277**: 11788–11794.

Journal of Controlled Release xxx (2012) xxx–xxx

Contents lists available at SciVerse ScienceDirect

Journal of Controlled Release

journal homepage: www.elsevier.com/locate/jconrel

Accumulation of arginine-rich cell-penetrating peptides in tumors and the potential for anticancer drug delivery *in vivo*

Ikuhiko Nakase [a], Yusuke Konishi [a], Masashi Ueda [b,c], Hideo Saji [c], Shiroh Futaki [a,*]

[a] *Institute for Chemical Research, Kyoto University, Kyoto 611–0011, Japan*
[b] *Faculty of Medicine, Radioisotopes Research Laboratory, Kyoto University Hospital, Kyoto University, Kyoto 606–8507, Japan*
[c] *Department of Patho-Functional Bioanalysis, Graduate School of Pharmaceutical Sciences, Kyoto University, Kyoto 606–8501, Japan*

ARTICLE INFO

Article history:
Received 18 June 2011
Accepted 13 January 2012
Available online xxxx

Keywords:
Arginine-rich cell-penetrating peptide
In vivo fluorescent imaging
Biodistribution
Tumor accumulation
Doxorubicin
Drug delivery

ABSTRACT

We investigated the biodistribution of arginine-rich cell-penetrating peptides (CPPs) in tumor-xenografted nude mice after intravenous injection of fluorescently labeled CPPs using *in vivo* imaging. The CPPs used included HIV-1 Tat (48–60), penetratin, and the L- and D-enantiomers of oligoarginines (8, 12, and 16 residues), all of which are reported to have high cell penetration. Among the tested peptides, high accumulation in tumors was observed for the D-form of octaarginine (r8), and glycosaminoglycans played a key role. Injection of an r8-doxorubicin conjugate (4 mg doxorubicin/kg) effectively suppressed tumor proliferation, with no significant decrease in mouse weight, whereas administration of doxorubicin itself (6 mg/kg), yielding a similar degree of tumor-growth suppression, resulted in significant weight loss. These results suggest the potential of r8 as a prototypic tumor-targeting vector.

1. Introduction

There is growing interest in peptides that can target tumor cells with sufficient specificity *in vivo*. Examples of such peptides include RGD (i.e., the Arg-Gly-Asp sequence that shows high affinity to integrin) [1,2], somatostatin [3–5], and bombesin [3,4,6], which target receptors that are overexpressed in tumors; applications in diagnosis, radiopeptide therapy, and targeted delivery have been reported. Phage display techniques have also been used to obtain novel peptides with a high specificity for cancers [7,8], and the isolation of homing peptides that recognize tumor-type-specific differences has also been reported [7,9]. However, the biodistribution, stability, and internalization efficiency of these homing peptides needs to be considerably improved [2,5,10].

Arginine-rich cell-penetrating peptides (CPPs), including Tat peptide (48–60 residues derived from human immunodeficiency virus (HIV-1) Tat protein) [11] and oligoarginine (derived from arginine residues 8–12) [12,13], have been reported to penetrate various types of cells efficiently without causing significant cytotoxicity [14]. Conjugation or complexation with CPPs can be used to deliver bioactive molecules, including proteins, nucleic acids, and various nanoparticles, into cells [14]. CPPs are thus promising vehicles for intracellular delivery. The conjugation of small-molecule therapeutics with arginine-rich CPPs may also be a powerful tool for overcoming multidrug resistance in tumor therapy [15]. For example, significant extension of the survival of ovarian-tumor-bearing mice was achieved by treatment with an octaarginine-Taxol conjugate [15].

The biodistributions of arginine-rich CPPs and their conjugates with bioactive cargoes reported to date often suggest preferential accumulation in the liver, kidney, lung, and spleen [e.g., [16–22]]. Due to the high ability of CPPs to penetrate cells, they are thought to have relatively low target-organ specificity, and their accumulation may depend mainly on the abundance of blood capillaries or macrophage-like cells in organs. Thus, strategies have been developed to use other cancer-targeting moieties together with CPPs to improve the intracellular delivery of anticancer agents [23–25]. Alternative approaches that use masking sequences with CPPs and harness the ability of CPPs to be activated in the vicinity of cancer cells have also been reported [26]. While successful cancer targeting has been reported using these strategies in combination with functional peptides, no study has extensively analyzed similarities and differences in biodistribution and possible accumulation among arginine-rich CPPs in cancerous tissues.

In this study, we investigated the biodistribution of a series of typical arginine-rich CPPs in tumor-xenografted nude mice after intravenous injection using Alexa660-labeled peptides and *in vivo* and *ex vivo* fluorescence imaging. The peptides used included HIV-1 Tat (48–60), penetratin, and the L- and D-forms of the oligoarginines (8, 12, and 16 mers). Large differences in accumulation in tumors were observed among the peptides, and the D-form of octaarginine (r8) showed the highest accumulation. Sustained retention over

* Corresponding author at: Institute for Chemical Research, Kyoto University, Uji, Kyoto 611–0011, Japan. Tel.: +81 774 38 3210; fax: +81 774 32 3038.
E-mail address: futaki@scl.kyoto-u.ac.jp (S. Futaki).

0168-3659/$ – see front matter © 2012 Elsevier B.V. All rights reserved.
doi:10.1016/j.jconrel.2012.01.016

24 h in tumor xenografts was observed. We also found that glycosaminoglycans played a key role in accumulation in tumors.

To assess the applicability of r8 for cancer therapy, a conjugate of doxorubicin with r8 (4 mg doxorubicin/kg) was prepared, which effectively suppressed tumor proliferation without decreasing mouse weight after intravenous injection. A higher dose of doxorubicin (6 mg/kg) was necessary to obtain the same extent of tumor growth suppression without conjugation to r8, but this was accompanied by significant weight loss.

2. Materials and methods

2.1. Peptide synthesis and fluorescent labeling

All the peptides employed in this study were chemically prepared by the 9-fluorenylmethyloxycarbonyl solid-phase peptide synthesis on a Rink amide resin as already described [27]. The amino acid derivatives and Rink amide resin (TGS-RAM) were purchased from the Peptide Institute (Osaka, Japan) and Shimadzu Biotech (Kyoto, Japan). Each arginine-rich peptide was designed to have a cysteine or glycyl cysteine amide at the C-terminus for the fluorescent labeling. Deprotection of the peptides and cleavage from the resin were conducted by treatment with a trifluoroacetic acid/ethanedithiol mixture (95:5) at room temperature for 3 h. Fluorescent labeling was conducted by treatment with 1.5 equivalents of Alexa Fluor 660 (alexa660) C2 maleimide sodium salt (Invitrogen, Eugene, OR, USA) in a dimethyl formamide/methanol mixture (1:1) for 1.5 h at room temperature followed by reverse-phase high-performance liquid chromatography purification. The structures of the synthesized peptides were confirmed by matrix-assisted laser desorption ionization time-of-flight mass spectrometry. Concentration of each peptide was adjusted based on the molar extinction coefficient at 668 nm ($112{,}000\ cm^{-1}\ M^{-1}$) [28].

2.2. Cell culture

Human cervical cancer-derived HeLa cells were purchased from the Riken BRC Cell Bank (Ibaraki, Japan) and cultured in α-minimal essential medium (α-MEM) containing 10% heat-inactivated bovine serum (Invitrogen). Chinese hamster ovary (CHO) cells [CHO-K1 cell lines, wild type; pgsA-745 (A-745) cell lines, all glycosaminoglycan deficient] were purchased from the American Type Culture Collection (Manassas, VA, USA), and cultured in an F-12 nutrient mixture (Ham's F-12) containing 10% heat-inactivated fetal bovine serum (Biological Industries, Kibbutz Beit Haemek, Israel). Cells were grown on 100-mm dishes and incubated at 37 °C under 5% CO_2.

2.3. Tumor-xenografted nude mouse

Animal studies were conducted in accordance with our institutional guidelines, and the experimental procedures were approved by the Kyoto University Animal Care Committee.

Female BALB/c nu/nu mice at 5 weeks of age were purchased from Japan SLC (Hamamatsu, Japan). HeLa (1.0×10^6 cells), CHO-K1 (4.0×10^6 cells), and A-745 (4.0×10^6 cells) were subcutaneously implanted into the shoulder of separate mice. The tumors were allowed to grow for ~2 weeks (HeLa) and ~4 weeks (CHO-K1 and A-745) to a volume of ~150 mm^3, then the *in vivo* studies were conducted.

2.4. In vivo and ex vivo fluorescent imaging

In vivo fluorescent imaging was conducted using an IVIS Spectrum System (Xenogen, CA, USA) at 1, 3, 6, 12, and 24 h after the tumor-xenografted mice were injected with alexa660-labeled CPPs (3 nmol in PBS) into the tail vein. During the imaging, the mice were kept on the imaging stage under anesthesia with 2.5% isoflurane gas in flowing oxygen. Fluorescent signals were detected using emission and excitation filters of 640 and 700 nm, respectively. *Ex vivo* imaging was also performed using the IVIS Spectrum System. When the mice were sacrificed at 24 h after the injection of the alexa660-labeled CPPs, fluorescent signals of each organ and the tumor were detected similar to the *in vivo* imaging.

2.5. Conjugation of CPPs to doxorubicin

The doxorubicin-maleimide compound was first prepared following the procedures reported by Furgeson et al. [29]. Doxorubicin (0.02 mmol) was dissolved in 5 mL of anhydrous methanol. *N*-(β-maleimidopropionic acid) hydrazide, trifluoroacetic acid salt (Pierce, Rockford, IL, USA) (0.04 mmol) was dissolved in 250 μL of anhydrous methanol and added to the doxorubicin solution. Two drops of trifluoroacetic acid were added to catalyze the Schiff-base formation of the hydrazide with the 13-keto position of the doxorubicin. The mixture was stirred at 20 °C for 4 h. Excess methanol was removed by rotary evaporation and the sample was purified by precipitation in anhydrous ethyl acetate. The purified samples were characterized by ^{1}H NMR and fast atom bombardment mass spectrometry.

The conjugation of the non-fluorescently labeled r8 [(D-Arg)$_8$-Gly-Cys-amide] with doxorubicin-maleimide was conducted by the treatment of the peptides with 1.5 equivalents of doxorubicin-maleimide in a dimethyl formamide/methanol mixture (1:1) for 1.5 h at room temperature followed by reverse-phase high-performance liquid chromatography purification. The structures of the synthesized peptides were confirmed by matrix-assisted laser desorption ionization time-of-flight mass spectrometry.

2.6. Tumor proliferation assay in vivo

After calculating tumor size (day 0; length × (width)^2/2, [24,30]), tumor-bearing mice were injected with the test compounds (2–6 mg/kg/day, dissolved in PBS) into the tail vein three times at 24 h intervals. After initial administration, tumor size was again estimated at 48 or 72 h intervals for up to 20 days. Body weights were measured similarly before and after injection of the test compounds. The average body weight of the mice was ~20 g; thus, the dose of 4 mg doxorubicin/kg corresponded to ~150 nmol r8-doxorubicin conjugate.

2.7. Cell viability

Cell viability was examined by MTT [3-(4,5-dimethylthyazol-2-yl)-2,5-diphenyltetrazolium bromide] assay as previously described [31]. Briefly, cells (5.0×10^3 cells/well) were cultured in 96-well microplates in α-MEM with 10% heat-inactivated bovine serum for 24 h. The cells were then incubated with the compounds (total volume, 50 μL) at 37 °C under 5% CO_2 for 24 h. MTT in PBS (0.05 mg/10 μL) was added to the above medium, and the cells were further incubated for 4 h. The precipitated MTT formazan was dissolved overnight in 0.04 N HCl in isopropanol (100 μL). The absorbance at 570 nm (A570) was then measured. Cell viability was expressed as the A570 ratio of the test compound-treated cells compared with cells incubated in the absence of the compounds.

2.8. Confocal microscopy and immunostaining

CHO-K1 cells and A-745 cells (4.0×10^5 cells/well) were plated on 35-mm glass-bottomed dishes (Iwaki, Tokyo, Japan) and cultured in Ham's F-12 medium containing 10% heat-inactivated fetal bovine serum for 48 h. After complete adhesion, the cells were washed with serum-free Ham's F-12 medium, and then the cells were incubated at 4 °C for 15 min in the medium (200 μL). The cells were

Please cite this article as: I. Nakase, et al., Accumulation of arginine-rich cell-penetrating peptides in tumors and the potential for anticancer drug delivery *in vivo*, J. Control. Release (2012), doi:10.1016/j.jconrel.2012.01.016

treated with anti-heparan sulfate antibody (10E4 epitope) (Seikagaku corporation, Tokyo, Japan) (1 μg/200 μL) at 4 °C for 30 min in serum-free Ham's F-12 medium, followed by washing the cells with PBS and the treatment of Alexa Fluor 488 (alexa488) goat anti-mouse IgM antibody (Invitrogen) (1 μg/200 μL) at 4 °C for 30 min in serum-free Ham's F-12 medium. Distribution of the fluorescent signals on the cell membranes was analyzed using an FV300 confocal scanning laser microscope (Olympus) equipped with a × 60 objective.

3. Results

3.1. Biodistribution of typical CPPs in tumor-xenografted mice after intravenous administration

We first examined the biodistribution of typical CPPs, including Tat peptide (amino acids 48–60 of HIV-1 Tat protein) [11], penetratin (Pen, derived from amino acids 43–58 of the Antennapedia homeoprotein) [32], and octaarginine (R8) composed of L-arginine [12,13] (Fig. 1A) in the tumor-xenografted nude mice with HeLa cells (derived from cervical cancer cells). These CPPs have been used as representative membrane-permeable carriers for efficient intracellular delivery [14]. For optical imaging, these CPPs were labeled with alexa660 at the cysteine residue located at their C-termini (Fig. 1A). Alexa660 may also be considered a model of a small molecular bioactive compound or anti-tumor agent to be delivered with the help of these CPPs. The GC peptide was used as a control to assess the effect of alexa660 on the biodistribution. Fluorescence images of mice 24 h after intravenous injection of the peptides (3 nmol) demonstrated that among the CPPs tested R8 accumulated the most (Fig. 1B). The distribution of each peptide in tumors and other organs was further analyzed in mice sacrificed 24 h after injection of each peptide (Fig. 1C). Compared to the control GC peptide, these CPPs showed relatively high accumulation in the kidney, liver, and lung. Interestingly, although the accumulations of Tat and Pen were only slightly different from that of the control GC peptide in tumors, that of R8 was significantly higher than the other peptides. In addition, compared to the control peptide, there were no significant differences in the accumulation of these CPPs in the blood, spleen, pancreas, heart, muscle, or brain at 24 h after administration. These results prompted us to study the biodistribution and tumor accumulation of the oligoarginine peptides further.

3.2. Effects of the number and configuration of arginine residues on the biodistribution of oligoarginine peptides in vivo

The number of arginine residues plays a critical role in determining the method of internalization and the internalization efficiencies of oligoarginine peptides. Thus, we synthesized alexa 660-labeled R2, R8, R12, and R16 peptides (Fig. 2A), and analyzed their biodistributions using an *in vivo* optical imager (Fig. 1B). R8 showed the highest accumulation in tumors at 24 h after administration (Fig. 2B). Substitution of peptide sequences by their D-enantiomers often increases the resistance of peptides to degradation by proteases. Thus, we prepared the D-enantiomer of the R8 peptide (r8) and examined its biodistribution and the extent of its accumulation in tumors. As a reference, the behavior of r12 (the D-enantiomer of R12) was also studied. Marked accumulation of r8 was observed in the tumor xenografts (Fig. 2B); it was almost three times higher than that of R8, and nine times higher than that of the control GC peptide (Fig. 2C). High accumulation of r12 was also observed, but it was similar to that of R8 and significantly less than that of r8. Interestingly, the degree of accumulation was not proportional to the internalization efficiencies of these compounds in cultured cells, in which the r12 peptide showed the highest internalization efficiency (Fig. S1 in Supplementary Content).

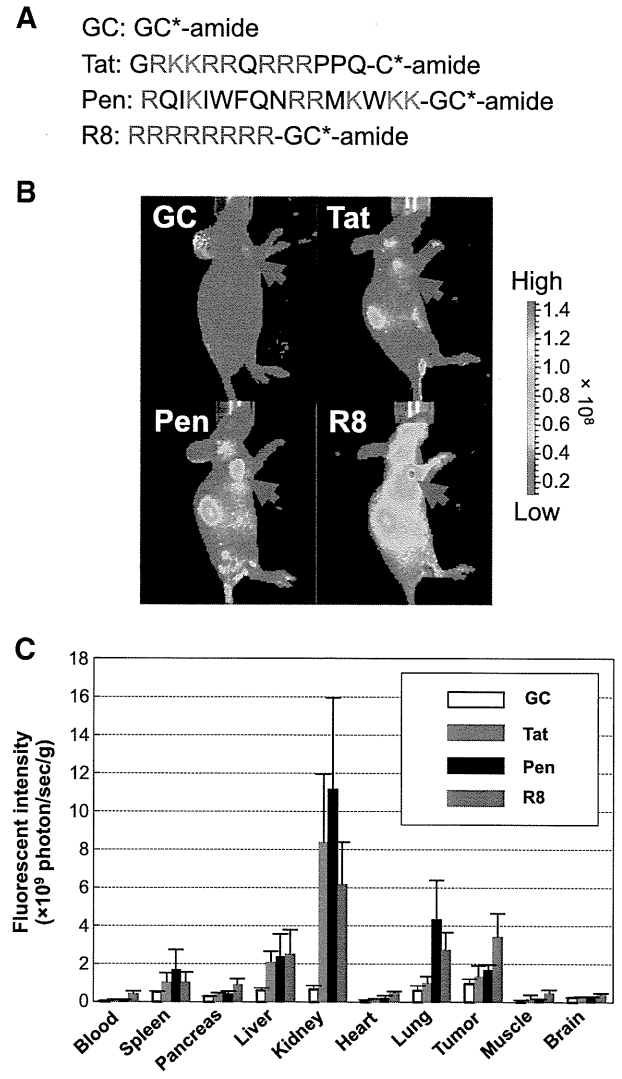

Fig. 1. Biodistribution of fluorescently labeled CPPs intravenously administrated into tumor-xenografted mice. (A) Structures of arginine-rich CPPs employed in this study. For the fluorescent labeling with alexa660, a cysteine (C) amide or glycyl-cysteine (GC) amide segment is attached to each peptide. The GC peptide that does not contain the CPP segments was employed as a control. C* denotes the alexa660-labeled cysteine. (B) *In vivo* fluorescent imaging of tumor-xenografted mice at 24 h after intravenous injection of alexa660-lebeled CPPs (3 nmol). Red arrows show tumor regions. (C) Fluorescent intensity of tumor and each organ. The mice were sacrificed at 24 h after the injection of the alexa660-lebeled GC (white), Tat (blue), penetratin (black), and R8 (red) peptides (3 nmol each), and then the fluorescent intensity of the tumor and each organ was analyzed using the IVIS Spectrum System. Data represent the average (± standard deviation (SD)) of five animals. (For interpretation of the references to color in this figure legend, the reader is referred to the web version of this article.)

3.3. Time-course of accumulation of oligoarginines in tumors after administration

To study the mechanism of accumulation of r8 in tumor xenografts further, the intensities of r8-alexa660 signals in tumor xenografts were analyzed sequentially together with the other oligoarginine peptides (Fig. 3). Data were obtained at 1, 3, 6, 12, and 24 h after injection of the peptide in mice, and the accumulation of the peptide in tumors and in muscle (control organ) was analyzed using optical imaging.

Compared to all other peptides, there was a marked accumulation of r8 in tumors at 1 h after injection, which decreased to ~30% at 24 h (Fig. 3D). The level of accumulation of r12 at 1 h after administration was almost half that of r8 (Fig. 3E). A time-dependent decrease in the

Please cite this article as: I. Nakase, et al., Accumulation of arginine-rich cell-penetrating peptides in tumors and the potential for anticancer drug delivery *in vivo*, J. Control. Release (2012), doi:10.1016/j.jconrel.2012.01.016

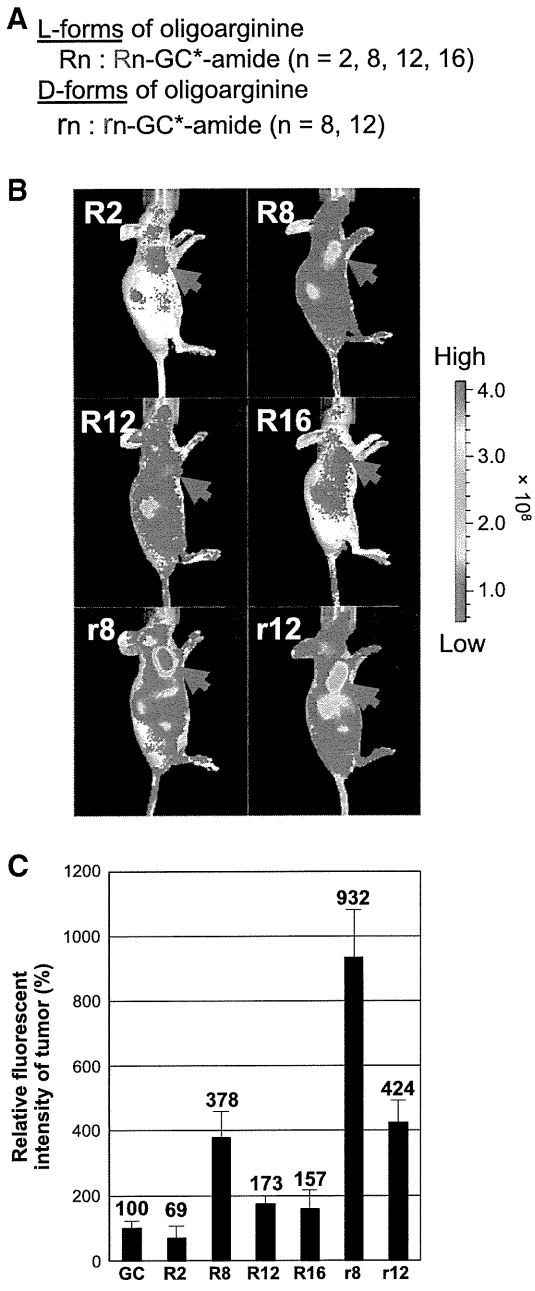

Fig. 2. Tumor accumulation of fluorescently labeled oligoarginine peptides intravenously administrated into tumor-bearing mice. (A) Structures of oligoarginine peptides bearing the GC-amide segment at the C-termini for the labeling with alexa660. R and r represent L- and D-arginines, respectively. C* denotes alexa660-labeled L-cysteine. (B) *In vivo* fluorescent imaging of tumor-xenografted mice at 24 h after intravenous injection of alexa660-labeled oligoarginine peptides (3 nmol each). Red arrows represent tumor xenografts. (C) Relative fluorescent intensity of tumor xenografts in B. The fluorescent intensity in tumor xenografts of mice treated with each peptide was adjusted based on the intrinsic fluorescence intensity before peptide administration. Data represent the average (±SD) of five animals. (For interpretation of the references to color in this figure legend, the reader is referred to the web version of this article.)

accumulation level was also observed for r12, yielding a ~20% retention of the r12 signal at 24 h. R12 showed similar accumulation to r12 at 1 h after administration. However, a steeper decrease in the signal level was observed for R12 (Fig. 3C). R8 had a less intense signal in tumors than did R12 at 1 h after administration, but it decreased at a slower rate than did R12 and at 24 h the signal was slightly higher than that of R12. Although GC-treated mice also showed a slight increase in fluorescence signal in tumors at 1 h after administration, the signal quickly decreased to the control level (Fig. 3A). The signals of peptides were significantly lower in muscle than in tumors at 1 h after administration, and the signals in muscle returned to control levels at 24 h (Fig. 3).

Time-course analyses showed that there was significantly more (~5-fold) r8 than R8 in blood at 1 h after intravenous injection. However, at 6 h after injection, r8 decreased to almost baseline levels, at which point levels were comparable to those of R8, suggesting higher retention of r8 in the blood (Supplementary Content Fig. S2).

3.4. Accumulation of oligoarginine peptides in organs

Twenty-four hours after intravenous administration of each fluorescently labeled oligoarginine peptide (3 nmol), the mice were sacrificed and fluorescence intensities in isolated organs and tumors were analyzed using an optical imaging system (Fig. 4). Among the CPPs tested, the signal of r8 in tumors was highest, as observed in the live imaging (Fig. 2). Similar accumulation of r8 in tumors was also observed in the liver and kidney (Fig. 4). Among the peptides tested, r12 accumulated the most in the liver (Fig. 4B). Compared to peptides composed of L-arginine, the retention of those with D-enantiomers was higher in tumors, presumably because of their resistance to proteases prior to their accumulation in the tumors [33].

3.5. Importance of glycosaminoglycans in the accumulation of r8 peptide in tumors

Membrane-associated proteoglycans, consisting of membrane proteins attached to sulfated disaccharide units called glycosaminoglycans (GAGs), play an important role in promoting the cellular uptake of arginine-rich CPPs [34,35]. On the other hand, high expression levels

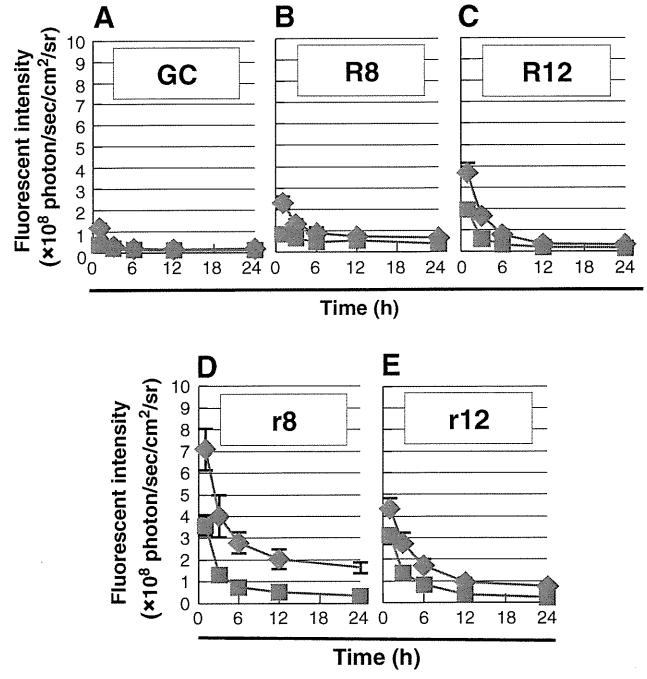

Fig. 3. Time-course study on accumulation of fluorescently labeled oligoarginine peptides in tumor (red) and muscle (blue). Tumor-xenografted mice were injected with each peptide (A, GC; B, R8; C, R12; D, r8; E, r12) (3 nmol each), and then *in vivo* fluorescent imaging of the mice was conducted at 1, 3, 6, 12, and 24 h after injection. Fluorescent intensity in tumor and muscle was analyzed using the IVIS Spectrum system. Data represent the average (±SD) of five animals. (For interpretation of the references to color in this figure legend, the reader is referred to the web version of this article.)

Please cite this article as: I. Nakase, et al., Accumulation of arginine-rich cell-penetrating peptides in tumors and the potential for anticancer drug delivery *in vivo*, J. Control. Release (2012), doi:10.1016/j.jconrel.2012.01.016

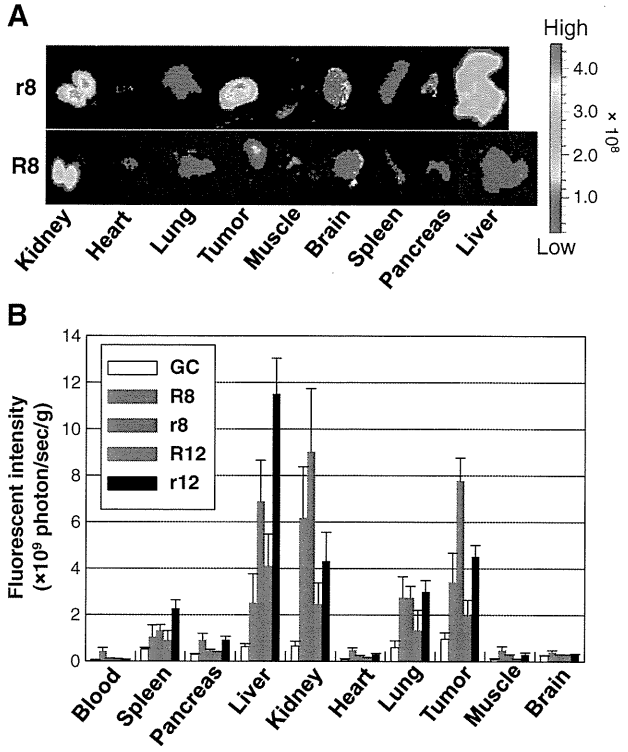

Fig. 4. Biodistribution of fluorescently labeled oligoarginine peptides administrated into tumor-xenografted mice. (A) Fluorescent imaging of each organ and tumor at 24 h after the mice were injected with r8- and R8-alexa660 (3 nmol each), then sacrificed. (B) Fluorescent intensity of tumor and each organ. The mice were sacrificed at 24 h after the injection of alexa660-lebeled GC (white), R8 (blue), r8 (red), R12 (green), and r12 (black) peptides (3 nmol each), and then the fluorescent intensity of the tumor and each organ was analyzed using the IVIS Spectrum system. Data represent the average (±SD) of five animals. (For interpretation of the references to color in this figure legend, the reader is referred to the web version of this article.)

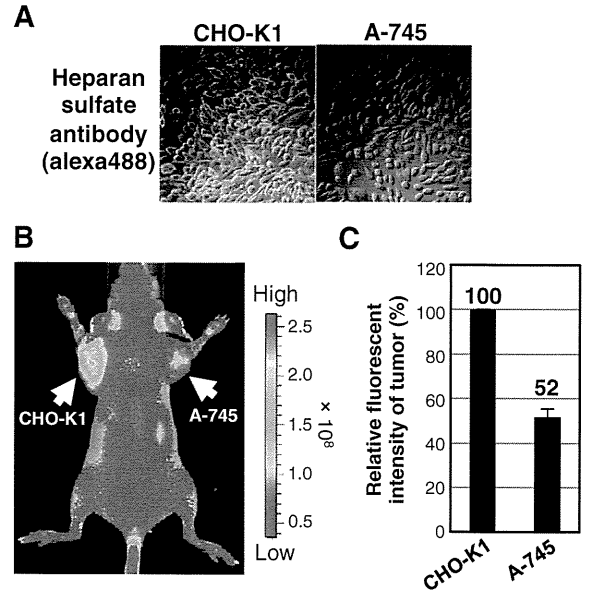

Fig. 5. Importance of glycosaminoglycans on the accumulation of r8 peptide in tumor. (A) Expression of heparan sulfate proteoglycans on cell surface of CHO-K1 and A-745 cells. The cells were stained with anti-heparan sulfate antibody labeled with alexa488. (B) *In vivo* fluorescent imaging of CHO-K1- and A-745-xenografted mice at 24 h after intravenous injection of r8-alexa660 (3 nmol). Arrows show tumor xenografts of CHO-K1 and A-745. (C) Relative fluorescent intensity of tumor xenografts of CHO-K1 and A-745 was analyzed using IVIS Spectrum system under the same conditions in B. Data represent the average (±SD) of three animals.

of proteoglycans have been reported in various cancer cells [36,37], as has the involvement of proteoglycans in various aspects of tumorigenesis, including cell adhesion, growth, and motility [37–39]. Thus, we next examined the importance of membrane-associated proteoglycans in the accumulation of r8-alexa660 in tumor xenografts *in vivo*. Wild-type CHO-K1 cells with membrane-associated proteoglycans, and A-745 cells deficient in GAGs (Fig. 5A), were implanted in the shoulders of nude mice. At 24 h after peptide administration (3 nmol), the fluorescence intensity of r8-alexa660 was higher in the CHO-K1 xenograft than in the A-745 xenograft (Fig. 5B, C), whereas that of alexa660-labeled albumin was almost the same in both xenografts (Supplementary Content Fig. S3). These results suggest that GAGs on plasma membranes may play an important role in the accumulation of r8 peptide in tumors.

3.6. Anticancer effect of r8-conjugated doxorubicin

Doxorubicin is widely used as a therapeutic anticancer agent [40–42]. However, the side effects of the drug, especially cardiotoxicity, are a major drawback [42–44]. To investigate the effects of the r8 peptide on the delivery of doxorubicin to a tumor, we prepared a conjugate of r8 and doxorubicin (r8-doxorubicin). A cross-link was formed between a cysteine introduced at the C-terminus of r8 and the 13-keto position of doxorubicin using maleimidopropionic acid hydrazide as a cross-linker, as reported by Furgeson et al. [29] (Fig. 6A). The hydrazone formed between doxorubicin and the cross-linker cleaves gradually at acidic pH and liberates doxorubicin [29,45,46]. We examined the anticancer activity of the conjugate by comparing it with free doxorubicin *in vitro* (Fig. 6B). Neither the r8-conjugate nor free doxorubicin showed significant suppression of tumor growth at 5 μM. However, higher cytotoxicity was seen with r8-doxorubicin than with doxorubicin itself when the cells were treated with 10 μM for 24 h at 37 °C, suggesting that the r8-conjugate did not hamper the anticancer activity of doxorubicin, but may have actually enhanced its activity (Fig. 6B). In addition, co-treatment with doxorubicin and the r8 peptide showed no significant effect on cytotoxicity (Fig. 6B).

The conjugate was then analyzed in an *in vivo* assay, based on tumor growth inhibition (Fig. 6C). Tumor-xenografted mice were injected with doxorubicin (4 or 6 mg/kg) or r8-doxorubicin (2 or 4 mg doxorubicin/kg) three times at 24 h intervals. Tumor volumes were measured before (day 0) and after administration, up to 21 days. The administration of 6 mg/kg doxorubicin resulted in a ~50% drop in tumor proliferation during the test period (Fig. 6C), but also a ~20% loss in body weight, suggesting high toxicity (Fig. 6D). No significant decrease in tumor growth was observed at the lower concentration of doxorubicin (4 mg/kg; Fig. 6C). Use of 4 mg doxorubicin/kg r8-doxorubicin led to similar inhibition to that of doxorubicin at 6 mg/kg (Fig. 6C), and no significant decrease in body weight (Fig. 6D). This suggests that conjugation of doxorubicin with r8 may maintain the required anticancer activity while reducing the side effects.

We additionally examined conjugates using an oligoarginine with lower internalization efficiencies. The D-form of the hexaarginine (r6) was used as a carrier peptide. Interestingly, although r6-alexa660 showed comparable tumor accumulation to that of r8-alexa660, the anti-tumor activity of r6-doxorubicin was not as high as that of the r8-conjugate (Supplementary Content Fig. S4).

4. Discussion

Several reports have suggested that arginine-rich CPPs and their conjugates tend to accumulate in certain organs, including the liver, kidney, lung, and spleen. However, few reports have studied the biodistribution of CPPs in tumor-xenografted mice. In the present study, using typical arginine-rich CPPs, we determined that there is a

Please cite this article as: I. Nakase, et al., Accumulation of arginine-rich cell-penetrating peptides in tumors and the potential for anticancer drug delivery *in vivo*, J. Control. Release (2012), doi:10.1016/j.jconrel.2012.01.016

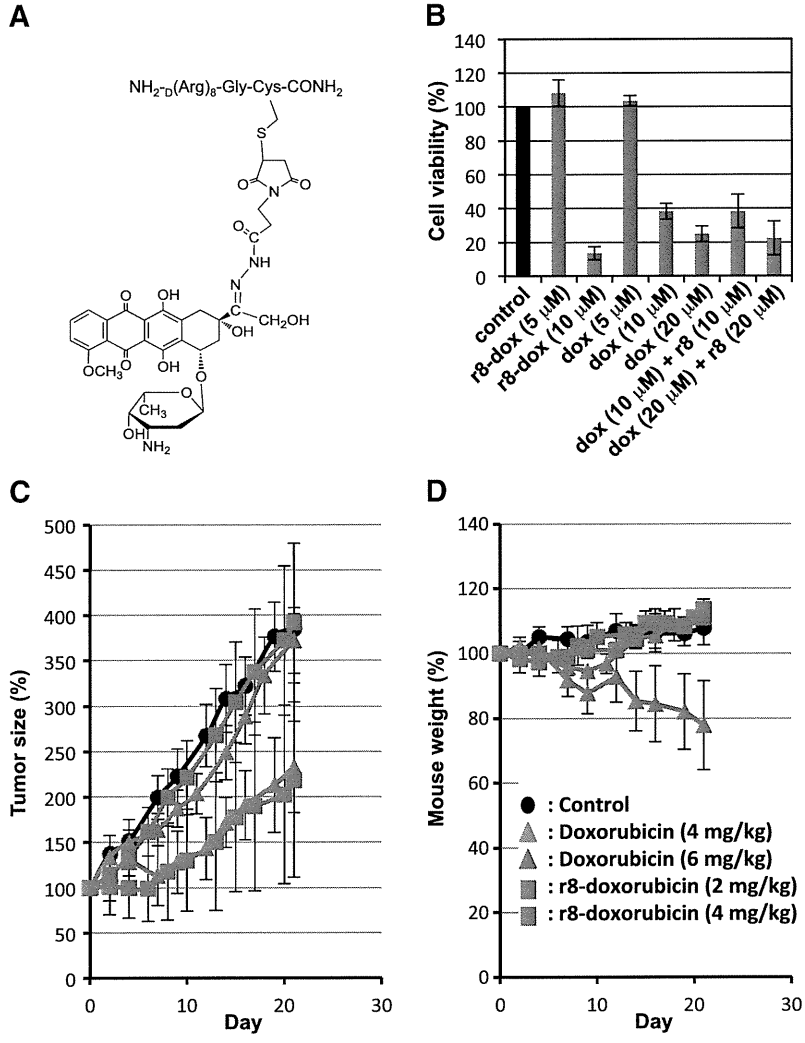

Fig. 6. Anticancer activity of the r8-doxorubicin conjugate. (A) Structure of the r8-doxorubicin conjugate. (B) Cytotoxicity of r8-doxorubicin (r8-dox) and doxorubicin (dox) *in vitro* assay. HeLa cells were treated with each test compound for 24 h at 37 °C, and then the MTT assay was conducted. (C, D) Tumor size (C) and body weight (D) of tumor-bearing mice treated with doxorubicin (4 mg/kg, orange; 6 mg/kg, blue), r8-doxorubicin (2 mg doxorubicin/kg, green; 4 mg doxorubicin/kg, red), and PBS (control, black). Data represent the average (±SD) of three (B) and five (C, D) experiments. (For interpretation of the references to color in this figure legend, the reader is referred to the web version of this article.)

considerable difference among peptides regarding their accumulation in tumors: Tat, Pen, and R8 showed a similar degree of accumulation in the kidney, liver, and lung. However, R8 showed higher accumulation in tumor xenografts. A comparison of oligoarginines composed of different numbers of arginines (R2, R8, R12, and R16) revealed that R8 accumulated the most in tumors, followed by R12. D-substitution of the amino acids of R8 and R12 increased accumulation further, where the level of r8 was almost nine-fold higher than that of the control GC peptide. A salient feature of r8 regarding its accumulation in tumors could be its prolonged retention in those tumors. It decreased by 6 h after injection, but this decrease quickly slowed and almost 70% of the level at 6 h remained at 24 h. This level of retention was significantly higher than that exhibited by the other oligoarginine peptides. At the same time, the accumulation levels of r8 in other organs were almost the same as those of the other oligoarginine peptides (slightly higher in the liver and kidney). These results indicate that r8 tends to accumulate more in tumors than do the other arginine-rich CPPs tested.

The detailed mechanism behind this tendency is currently unknown. However, assuming that arginine-rich CPPs composed of D-amino acids may be less susceptible to proteolysis than their L-isomers and that certain numbers of arginine residues are needed to efficiently interact with tumor cells, the prolonged retention of the D-isomer peptide structures may favor their accumulation in tumors. The higher retention of r8 peptide than R8 in the blood in the early phase after injection may further support this. Interestingly, r12 showed less marked accumulation in tumors than did r8. Compared to r8, r12 may interact more strongly with other organs, including the liver and lung, before arriving at a tumor. Retention of r12 in these organs may result in less accumulation in the tumor. On the other hand, to improve the pharmacokinetic profiles of doxorubicin and other anticancer agents, various formulations have already been reported that provide active [47,48] and passive tumor targeting using the enhanced permeation and retention (EPR) effect [48–50]. Accumulation of serum proteins in solid tumors has also been attributed to the EPR effect [48–50]. Oligoarginine peptides can thus be delivered into tumor tissues by binding to serum proteins. Leakage of the complexes through blood vessels into cancer tissues should result in the transfer of these peptides from serum proteins to tumor-related molecules having higher affinities for these peptides (e.g., proteoglycans), and a certain proportion of oligoarginines would then be trapped by the cancer cells. That r8 showed the highest accumulation in tumor tissues may be explained in terms of its stability in blood and affinity for serum proteins and tumor tissues. L-forms of

Please cite this article as: I. Nakase, et al., Accumulation of arginine-rich cell-penetrating peptides in tumors and the potential for anticancer drug delivery *in vivo*, J. Control. Release (2012), doi:10.1016/j.jconrel.2012.01.016

oligoarginines are more susceptible to proteolytic enzymes than D-peptides. Degradation of the peptides results in decreased binding affinity for serum proteins as well as less accumulation in tumor tissues. Although r12 was more efficiently taken up by the cells than r8, this peptide also has a higher affinity for serum proteins [51]. This leads to strong retention of r12 by serum proteins when delivered into tumor tissues, whereas r8 fractionated into tumor tissues more readily.

We also found significant *in vivo* accumulation of r8 in wild-type CHO-K1 xenografts but not in GAG-deficient A-745 xenografts. Consistent with the superior *in vitro* cellular uptake of arginine-rich CPPs by CHO-K1 cells versus A-745 cells, the serum-bound r8 should be transferred more favorably to the former xenografts. High expression of proteoglycans in various tumor cells has already been reported [36,37], and the involvement of GAGs in tumor development, including angiogenesis and metastasis, has been suggested [37–39]. Thus, the interaction of r8 with tumor-associated GAGs may promote its accumulation in tumors. In addition, there was no significant difference in accumulation of alexa660-labeled albumin in CHO-K1 and A-745 cells, suggesting that an EPR effect cannot solely explain the accumulation of r8 in tumors and that fractionation of oligoarginines from serum to tumor tissues may be another important factor.

The potential of r8 to deliver an anticancer agent was also assessed using doxorubicin as a model compound (Fig. 6). Doxorubicin is an anthracycline antibiotic that is widely used as an anticancer agent [40–42]. However, the systemic administration of doxorubicin can lead to severe cardiac toxicity [42–44]. In this study, we prepared a conjugate of doxorubicin with r8 and examined the feasibility of the r8-conjugate for tumor treatment. Free doxorubicin can permeate plasma membranes by itself and often shows higher anti-tumor activity than when it is conjugated with carrier molecules. However, in this study, free doxorubicin and r8-doxorubicin exhibited similar anti-tumor activities. This could be because r8 has high membrane permeability and high affinity for cellular DNA and RNA; binding of r8 to cellular nucleic acids may increase the affinity of doxorubicin for its target in the cells and enhance bioactivity.

While 6 mg/kg doxorubicin effectively suppressed tumor growth in mice, this was accompanied by significant weight loss, suggesting strong side effects of doxorubicin. On the other hand, administration of r8-doxorubicin (4 mg doxorubicin/kg) resulted in suppression of tumor proliferation to the same extent as doxorubicin (6 mg/kg), but without causing significant weight loss. Thus, conjugation with r8 may enhance the activity of anticancer agents, making it possible to use lower doses of agents and thereby reduce the side effects. Although r6-alexa660 and r8-alexa660 showed similar degrees of accumulation in tumors, r6-doxorubicin showed less anti-tumor proliferation activity than did r8-doxorubicin. This may be because r6 has a lower affinity for serum proteins and therefore is more easily liberated from serum proteins, whereas its affinity to the acceptors (e.g., tumor-tissue-associated GAGs) is also lower than that of r8. Thus, the retention of r6 in tumor tissues may be almost the same as that of r8. On the other hand, the internalization efficiency of r6 in tumor cells appears to be lower than that of r8, and this may eventually result in the lower anti-tumor activity of r6-doxorubicin than that of the r8-conjugate. Thus, the anti-tumor activity of r8-doxorubicin should be analyzed in terms of a balance between serum binding, affinity for tumor tissue, and internalization efficiency.

In conclusion, our study demonstrates that D-form octaarginine (r8) accumulates in high levels in tumor tissues. Our study was intended to obtain basic information about the *in vivo* distribution of oligoarginine peptides in tumor-xenografted mice. Further studies are needed to assess the utility of using r8 to target different types of cancer cells as well as the feasibility of the simple conjugation of r8 for practical cancer therapy. Such information could lead to more effective and sophisticated delivery systems for anticancer therapies. The present results may provide a novel starting point for the design of tumor-targeting therapeutic and diagnostic systems.

Acknowledgement

We are grateful for skillful assistance in experiments using NMR spectroscopy by Tomoyuki Yoshimura. This work was supported in part by Grants-in-Aid for Scientific Research from the Ministry of Education, Culture, Sports, Science and Technology of Japan and the Ministry of Health Labour and Welfare of Japan.

Appendix A. Supplementary data

Supplementary data to this article can be found online at doi:10.1016/j.jconrel.2012.01.016.

References

[1] E. Ruoslahti, M.D. Pierschbacher, New perspectives in cell adhesion: RGD and integrins, Science 238 (1987) 491–497.
[2] S. Liu, Radiolabeled cyclic RGD peptides as integrin alpha(v)beta(3)-targeted radiotracers: maximizing binding affinity via bivalency, Bioconjug. Chem. 20 (2009) 2199–2213.
[3] A.V. Schally, A. Nagy, New approaches to treatment of various cancers based on cytotoxic analogs of LHRH, somatostatin and bombesin, Life Sci. 72 (2003) 2305–2320.
[4] S.M. Okarvi, Peptide-based radiopharmaceuticals and cytotoxic conjugates: potential tools against cancer, Cancer Treat. Rev. 34 (2008) 13–26.
[5] S.E. Pool, E.P. Krenning, G.A. Koning, C.H. van Eijck, J.J. Teunissen, B. Kam, R. Valkema, D.J. Kwekkeboom, M. de Jong, Preclinical and clinical studies of peptide receptor radionuclide therapy, Semin. Nucl. Med. 40 (2010) 209–218.
[6] X.L. Wang, R. Xu, Z.R. Lu, A peptide-targeted delivery system with pH-sensitive amphiphilic cell membrane disruption for efficient receptor-mediated siRNA delivery, J. Control. Release 134 (2009) 207–213.
[7] J. Enbäck, P. Laakkonen, Tumour-homing peptides: tools for targeting, imaging and destruction, Biochem. Soc. Trans. 35 (2007) 780–783.
[8] A. Rivinoja, P. Laakkonen, Identification of homing peptides using the in vivo phage display technology, Meth. Mol. Biol. 683 (2011) 401–415.
[9] W. Tai, R. Mahato, K. Cheng, The role of HER2 in cancer therapy and targeted drug delivery, J. Control. Release 146 (2010) 264–275.
[10] V. Askoxylakis, S. Zitzmann-Kolbe, F. Zoller, A. Altmann, A. Markert, S. Rana, A. Marr, W. Mier, J. Debus, U. Haberkorn, Challenges in optimizing a prostate carcinoma binding peptide, identified through the phage display technology, Molecules 16 (2011) 1559–1578.
[11] E. Vivès, P. Brodin, B. Lebleu, A truncated HIV-1 Tat protein basic domain rapidly translocates through the plasma membrane and accumulates in the cell nucleus, J. Biol. Chem. 272 (1997) 16010–16017.
[12] J.B. Rothbard, S. Garlington, Q. Lin, T. Kirschberg, E. Kreider, P.L. McGrane, P.A. Wender, P.A. Khavari, Conjugation of arginine oligomers to cyclosporin A facilitates topical delivery and inhibition of inflammation, Nat. Med. 6 (2000) 1253–1257.
[13] S. Futaki, T. Suzuki, W. Ohashi, T. Yagami, S. Tanaka, K. Ueda, Y. Sugiura, Arginine-rich peptides. An abundant source of membrane-permeable peptides having potential as carriers for intracellular protein delivery, J. Biol. Chem. 276 (2001) 5836–5840.
[14] Special Theme Issue on Membrane Permeable Peptide Vectors: Chemistry and Functional Design for the Therapeutic Applications, S. Futaki (Ed.), Adv. Drug Deliv. Rev., vol. 60, 2008, pp. 447–614.
[15] E.A. Dubikovskaya, S.H. Thorne, T.H. Pillow, C.H. Contag, P.A. Wender, Overcoming multidrug resistance of small-molecule therapeutics through conjugation with releasable octaarginine transporters, Proc. Natl. Acad. Sci. U. S. A. 105 (2008) 12128–12133.
[16] S. Fawell, J. Seery, Y. Daikh, C. Moore, L.L. Chen, B. Pepinsky, J. Barsoum, Tat-mediated delivery of heterologous proteins into cells, Proc. Natl. Acad. Sci. U. S. A. 91 (1994) 664–668.
[17] S.R. Schwarze, A. Ho, A. Vocero-Akbani, S.F. Dowdy, In vivo protein transduction: delivery of a biologically active protein into the mouse, Science 285 (1999) 1569–1572.
[18] H.J. Lee, W.M. Pardridge, Pharmacokinetics and delivery of tat and tat-protein conjugates to tissues in vivo, Bioconjug. Chem. 12 (2001) 995–999.
[19] K.E. Bullok, M. Dyszlewski, J.L. Prior, C.M. Pica, V. Sharma, D. Piwnica-Worms, Characterization of novel histidine-tagged Tat-peptide complexes dual-labeled with (99m)Tc-tricarbonyl and fluorescein for scintigraphy and fluorescence microscopy, Bioconjug. Chem. 13 (2002) 1226–1237.
[20] P. Wunderbaldinger, L. Josephson, R. Weissleder, Tat peptide directs enhanced clearance and hepatic permeability of magnetic nanoparticles, Bioconjug. Chem. 13 (2002) 264–268.
[21] S. Kameyama, R. Okada, T. Kikuchi, T. Omura, I. Nakase, T. Takeuchi, Y. Sugiura, S. Futaki, Distribution of immunoglobulin Fab fragment conjugated with HIV-1 REV

peptide following intravenous administration in rats, Mol. Pharm. 3 (2006) 174–180.
[22] S. Kameyama, M. Horie, T. Kikuchi, T. Omura, T. Takeuchi, I. Nakase, Y. Sugiura, S. Futaki, Effects of cell-permeating peptide binding on the distribution of 125I-labeled Fab fragment in rats, Bioconjug. Chem. 17 (2006) 597–602.
[23] E.L. Snyder, B.R. Meade, C.C. Saenz, S.F. Dowdy, Treatment of terminal peritoneal carcinomatosis by a transducible p53-activating peptide, PLoS Biol. 2 (2004) E36.
[24] M. Tan, K.H. Lan, J. Yao, C.H. Lu, M. Sun, C.L. Neal, J. Lu, D. Yu, Selective inhibition of ErbB2-overexpressing breast cancer in vivo by a novel TAT-based ErbB2-targeting signal transducers and activators of transcription 3-blocking peptide, Cancer Res. 66 (2006) 3764–3772.
[25] S. Kizaka-Kondoh, S. Itasaka, L. Zeng, S. Tanaka, T. Zhao, Y. Takahashi, K. Shibuya, K. Hirota, G.L. Semenza, M. Hiraoka, Selective killing of hypoxia-inducible factor-1-active cells improves survival in a mouse model of invasive and metastatic pancreatic cancer, Clin. Cancer Res. 15 (2009) 3433–3441.
[26] E.S. Olson, T. Jiang, T.A. Aguilera, Q.T. Nguyen, L.G. Ellies, M. Scadeng, R.Y. Tsien, Activatable cell penetrating peptides linked to nanoparticles as dual probes for in vivo fluorescence and MR imaging of proteases, Proc. Natl. Acad. Sci. U. S. A. 107 (2010) 4311–4316.
[27] S. Futaki, M. Niwa, I. Nakase, A. Tadokoro, Y. Zhang, M. Nagaoka, N. Wakako, Y. Sugiura, Arginine carrier peptide bearing Ni(II) chelator to promote cellular uptake of histidine-tagged proteins, Bioconjug. Chem. 15 (2004) 475–481.
[28] R.P. Haugland, Handbook of Fluorescent Probes and Research Products, ninth edition Molecular Probes Inc, 2002.
[29] D.Y. Furgeson, M.R. Dreher, A. Chilkoti, Structural optimization of a "smart" doxorubicin-polypeptide conjugate for thermally targeted delivery to solid tumors, J. Control. Release 110 (2006) 362–369.
[30] K. Sano, T. Temma, T. Azuma, R. Nakai, M. Narazaki, Y. Kuge, H. Saji, A Pre-targeting Strategy for MR Imaging of Functional Molecules Using Dendritic Gd-Based Contrast Agents, Mol. Imaging Biol. 13 (2011) 1196–1203.
[31] I. Nakase, M. Niwa, T. Takeuchi, K. Sonomura, N. Kawabata, Y. Koike, M. Takehashi, S. Tanaka, K. Ueda, J.C. Simpson, A.T. Jones, Y. Sugiura, S. Futaki, Cellular uptake of arginine-rich peptides: roles for macropinocytosis and actin rearrangement, Mol. Ther. 10 (2004) 1011–1022.
[32] D. Derossi, A.H. Joliot, G. Chassaing, A. Prochiantz, The third helix of the Antennapedia homeodomain translocates through biological membranes, J. Biol. Chem. 269 (1994) 10444–10450.
[33] R. Bessalle, A. Kapitkovsky, A. Gorea, I. Shalit, M. Fridkin, All-D-magainin: chirality, antimicrobial activity and proteolytic resistance, FEBS Lett. 274 (1990) 151–155.
[34] I. Nakase, A. Tadokoro, N. Kawabata, T. Takeuchi, H. Katoh, K. Hiramoto, M. Negishi, M. Nomizu, Y. Sugiura, S. Futaki, Interaction of arginine-rich peptides with membrane-associated proteoglycans is crucial for induction of actin organization and macropinocytosis, Biochemistry 46 (2007) 492–501.
[35] I. Nakase, H. Hirose, G. Tanaka, A. Tadokoro, S. Kobayashi, T. Takeuchi, S. Futaki, Cell-surface accumulation of flock house virus-derived peptide leads to efficient internalization via macropinocytosis, Mol. Ther. 17 (2009) 1868–1876.
[36] K. Matsuda, H. Maruyama, F. Guo, J. Kleeff, J. Itakura, Y. Matsumoto, A.D. Lander, M. Korc, Glypican-1 is overexpressed in human breast cancer and modulates the mitogenic effects of multiple heparin-binding growth factors in breast cancer cells, Cancer Res. 61 (2001) 5562–5569.
[37] J.H. Lee, H. Park, H. Chung, S. Choi, Y. Kim, H. Yoo, T.Y. Kim, H.J. Hann, I. Seong, J. Kim, K.G. Kang, I.O. Han, E.S. Oh, Syndecan-2 regulates the migratory potential of melanoma cells, J. Biol. Chem. 284 (2009) 27167–27175.
[38] R.D. Sanderson, Heparan sulfate proteoglycans in invasion and metastasis, Semin. Cell Dev. Biol. 12 (2001) 89–98.
[39] I. Vlodavsky, O. Goldshmidt, E. Zcharia, R. Atzmon, Z. Rangini-Guatta, M. Elkin, T. Peretz, Y. Friedmann, Mammalian heparanase: involvement in cancer metastasis, angiogenesis and normal development, Semin. Cancer Biol. 12 (2002) 121–129.
[40] R.L. Momparler, M. Karon, S.E. Siegel, F. Avila, Effect of adriamycin on DNA, RNA, and protein synthesis in cell-free systems and intact cells, Cancer Res. 36 (1976) 2891–2895.
[41] C.A. Frederick, L.D. Williams, G. Ughetto, G.A. van der Marel, J.H. van Boom, A. Rich, A.H. Wang, Structural comparison of anticancer drug-DNA complexes: adriamycin and daunomycin, Biochemistry 29 (1990) 2538–2549.
[42] D.A. Gewirtz, A critical evaluation of the mechanisms of action proposed for the antitumor effects of the anthracycline antibiotics adriamycin and daunorubicin, Biochem. Pharmacol. 57 (1999) 727–741.
[43] M.J. Aiken, V. Suhag, C.A. Garcia, E. Acio, S. Moreau, D.A. Priebat, S.P. Chennupati, D. Van Nostrand, Doxorubicin-induced cardiac toxicity and cardiac rest gated blood pool imaging, Clin. Nucl. Med. 34 (2009) 762–767.
[44] Y.W. Zhang, J. Shi, Y.J. Li, L. Wei, Cardiomyocyte death in doxorubicin-induced cardiotoxicity, Arch. Immunol. Ther. Exp. (Warsz.) 57 (2009) 435–445.
[45] T. Kaneko, D. Willner, I. Monkovíc, J.O. Knipe, G.R. Braslawsky, R.S. Greenfield, D.M. Vyas, New hydrazone derivatives of adriamycin and their immunoconjugates-a correlation between acid stability and cytotoxicity, Bioconjug. Chem. 2 (1991) 133–141.
[46] S. Cai, S. Thati, T.R. Bagby, H.M. Diab, N.M. Davies, M.S. Cohen, M.L. Forrest, Localized doxorubicin chemotherapy with a biopolymeric nanocarrier improves survival and reduces toxicity in xenografts of human breast cancer, J. Control. Release 146 (2010) 212–218.
[47] T.M. Allen, Ligand-targeted therapeutics in anticancer therapy, Nat. Rev. Cancer 2 (2002) 750–763.
[48] F. Danhier, O. Feron, V. Préat, To exploit the tumor microenvironment: passive and active tumor targeting of nanocarriers for anti-cancer drug delivery, J. Control. Release 148 (2010) 135–146.
[49] Y. Matsumura, H. Maeda, A new concept for macromolecular therapeutics in cancer chemotherapy: mechanism of tumoritropic accumulation of proteins and the antitumor agent smancs, Cancer Res. 46 (1986) 6387–6392.
[50] H. Maeda, J. Wu, T. Sawa, Y. Matsumura, K. Hori, Tumor vascular permeability and the EPR effect in macromolecular therapeutics: a review, J. Control. Release 65 (2000) 271–284.
[51] M. Kosuge, T. Takeuchi, I. Nakase, A.T. Jones, S. Futaki, Cellular internalization and distribution of arginine-rich peptides as a function of extracellular peptide concentration, serum, and plasma membrane associated proteoglycans, Bioconjug. Chem. 19 (2008) 656–664.

Please cite this article as: I. Nakase, et al., Accumulation of arginine-rich cell-penetrating peptides in tumors and the potential for anticancer drug delivery *in vivo*, J. Control. Release (2012), doi:10.1016/j.jconrel.2012.01.016